ARTICLE
Traditional Medicine Research 2026;11(3):18. http://doi.org/10.53388/TMR20250407002

Multi-analytical characterization of *Os Draconis*: distinguishing authentic samples from fossilized specimens and counterfeits for improved authentication

Dong-Han Bai[1], Lu Luo[1,2*], Zi-Hao Zhang[3], Zi Xing[1, 4], Remy Macdonald[5], Shu-Min Chen[6], Qiao-Chu Wang[3], Zhi-Jie Zhang[1]

[1]Institute of Chinese Materia Medica, China Academy of Chinese Medical Sciences, Beijing 100700, China. [2]Pharmacological and Pharmaceutical Sciences, College of Pharmacy, University of Houston, Houston 77030, USA. [3]Department of Biochemistry and Molecular and Cellular Biology, Georgetown University, Washington DC 20057, USA. [4]Review Department II, Shandong Center For Food and Drug Evaluation & Inspection, Ji'nan 250014, China. [5]Department of Statistics, George Mason University, Fairfax 22030, USA. [6]Institute of Acupuncture and Moxibustion, China Academy of Chinese Medical Sciences, Beijing 100700, China.

[*]**Correspondence to:** Lu Luo, Institute of Chinese Materia Medica, China Academy of Chinese Medical Sciences, No. 16, Dongzhimen Nei Nan Xiaojie, Dongcheng District, Beijing 100700, China. E-mail: lluo@icmm.ac.cn.

Author contributions

Luo L supervised and administered the project, conducted the investigation, performed the validation, and reviewed and edited the manuscript. Bai DH conducted the experiments and reviewed and edited the manuscript. Zhang ZH generated the figures and reviewed and edited the manuscript. Xing Z collected the data and reviewed and edited the manuscript. Macdonald M performed the data analysis and reviewed and edited the manuscript. Chen SM collected the samples and reviewed and edited the manuscript. Wang QC conducted the experiments, collected the data, and reviewed and edited the manuscript. Zhang ZJ curated the data, acquired the funding, and reviewed and edited the manuscript.

Competing interests

The authors declare no conflicts of interest.

Acknowledgments

This project was supported by the Scientific and Technological Innovation Project of the China Academy of Chinese Medical Sciences (CI2021A04013), the National Natural Science Foundation of China (82204610), the Qihang Talent Program (L2022046), and the Fundamental Research Funds for the Central Public Welfare Research Institutes (ZZ15-YQ-041 and L2021029). We express our gratitude for their financial support, which made this research possible.

Peer review information

Traditional Medicine Research thanks Yue-Ping Jiang, Cheng-Hao Fei and another anonymous reviewer for their contribution to the peer review of this paper.

Abbreviations

^{14}C, radiocarbon dating; ANOVA, analysis of variance; EPMA, electron probe microanalysis; FTIR, fourier-transform infrared spectroscopy; HAP, hydroxyapatite; ICP-MS, inductively coupled plasma mass spectrometry; PLM, polarizing light microscopy; TCM, traditional Chinese medicine; XRD, X-ray diffraction.

Citation

Bai DH, Luo L, Zhang ZH, et al. Multi-analytical characterization of *Os Draconis*: distinguishing authentic samples from fossilized specimens and counterfeits for improved authentication. *Tradit Med Res*. 2026;11(3):18. doi: 10.53388/TMR20250407002.

Production editor: Meng-Meng Song.

Received: 07 April 2025; **Revised:** 16 May 2025; **Accepted:** 20 November 2025; **Available online:** 21 November 2025.

Abstract

Background: *Os Draconis* is an important material in traditional Chinese medicine (TCM). However, its market is saturated with counterfeit products, and the limitations of current identification methods pose a serious threat to clinical effectiveness and drug safety. This study aims to establish a more accurate and comprehensive authentication system for *Os Draconis*. **Methods:** A comprehensive approach was employed to analyze authentic *Os Draconis*, fossilized *Os Draconis*, counterfeit products, and lab-prepared modern animal bones. The analytical techniques included ^{14}C dating, electron probe microanalysis (EPMA), polarized light microscopy, X-ray diffraction (XRD), inductively coupled plasma mass spectrometry (ICP-MS), and fourier-transform infrared spectroscopy (FTIR). The study focused on examining the microstructural features and micro-area elemental compositions to identify distinguishing characteristics. **Results:** Physical identification alone was insufficient to reliably distinguish authentic *Os Draconis* from its counterfeits. XRD analysis revealed that while hydroxyapatite is the main component in all samples, authentic *Os Draconis* also contains calcium carbonate and quartz, which were absent in counterfeit and lab-prepared samples. FTIR spectra identified the carbonate ion (CO_3^{2-}) as a characteristic infrared marker for authentic *Os Draconis*. ICP-MS analysis showed that Ca and P are the major elements, with a notably high content of Lanthanum (La) among rare earth elements in authentic samples. The EPMA results demonstrated that the Ca/P ratio of authentic *Os Draconis* is distinct, falling between that of fossilized *Os Draconis* and counterfeit samples. **Conclusion:** This study successfully identified several precise markers, including the presence of calcium carbonate, the characteristic CO_3^{2-} infrared peak, a high La content, and a specific Ca/P ratio, for the accurate and rapid authentication of *Os Draconis*. Furthermore, the analysis of its natural porous structure, suitable pore size, and surface area suggests that *Os Draconis* has significant potential as a natural drug carrier.

Keywords: *Os Draconis*; ultrastructure; ^{14}C dating; EPMA; XRD; ICP-MS; FTIR

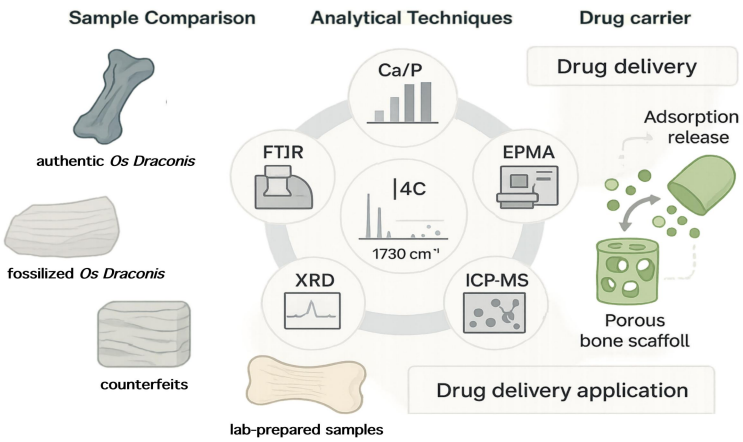

Traditional Medicine Research 2026;11(3):18. http://doi.org/10.53388/TMR20250407002

Highlights

1. Physicochemical analysis combining XRD and FTIR confirms that the primary component of *Os Draconis* (Longgu) is hydroxyapatite, consistent with its origin as fossilized bone.
2. A comprehensive analytical strategy integrating multiple techniques (PLM, EPMA, ICP-MS) provides a robust standard for distinguishing authentic Longgu from common adulterants.
3. Radiocarbon dating (^{14}C) and trace element profiling offer a novel approach to ascertain the fossil age and potential geographical provenance of Longgu samples, enhancing quality control.

Medical history of objective

Os Draconis (Longgu), commonly known as Dragon's Bone, was first documented in *Shennong Bencao Jing,* which was compiled during the late Western Han Dynasty. Its properties and applications were further detailed and expanded upon in the *Compendium of Materia Medica*, compiled by Shizhen Li of the Ming Dynasty (published 1596 C.E.). Traditionally, its primary efficacies are to sedate the heart and calm the spirit, pacify the liver and "subdue yang" (calm excessive yang, where Yang represents the dynamic, active, and heat-generating aspects of the body's energy, such as mental excitability and physical restlessness), and to astringe and consolidate. It is historically prescribed for conditions such as palpitations with anxiety, insomnia, epilepsy, dizziness, spontaneous sweating, and chronic discharges. Modern research suggests that its rich content of calcium phosphate, calcium carbonate, and various trace elements may be responsible for its sedative, anticonvulsant, and antacid pharmacological effects.

Introduction

As a distinctive part of traditional Chinese medicine (TCM), mineral medicines include unique fossil-based materials such as *Os Draconis*. This material, referred to as Longgu or "dragon bone", is frequently employed in TCM for managing emotional disorders. It has shown significant therapeutic value for a range of conditions including anxiety, insomnia, and various forms of depression, particularly those that co-occur with other chronic illnesses or arise from significant life events. [1–4]. These studies demonstrate favorable outcomes when *Os Draconis* formulas are used to treat various depression-related conditions. Clinically, numerous doctors and researchers have adapted Chaihu Longgu Muli Tang (*Bupleuri Radix*, *Os Draconis*, and *Ostreae Concha*) for treating coronary heart disease patients with comorbid depression and anxiety. Studies concluded that it has fewer adverse effects and higher safety compared to conventional Western treatments [5–7]. Internationally, Japan has developed Chaihu Longgu Muli Tang as an antidepressant, sparking extensive research on the decoction's antidepressant effects [8–12].

Os Draconis refers to fossilized bones of ancient mammals such as three-toed horses, rhinoceroses, deer, cattle, elephants, or the fossilized tusks of elephants [13]. Compared to traditional studies, modern TCM research has employed a range of scientific techniques to analyze traditional medicines [14–17]. Studies indicate that *Os Draconis*'s raw minerals are composed of apatite, calcite, and trace clay minerals [18]. It primarily contains calcium carbonate and calcium phosphate, along with trace elements such as iron, potassium, and sodium [19]. Additionally, it contains seven amino acids, including glycine, cystine, methionine, isoleucine, leucine, tyrosine, and phenylalanine. It also contains trace elements like zinc, copper, manganese, iron, molybdenum, cobalt, chromium, nickel, and selenium. Harmful elements such as heavy metals – copper, chromium, cadmium, arsenic, and lead – and radioactive elements like uranium and thorium are also present [20, 21]. Current research shows that its main component is hydroxyapatite, which is also the primary component of animal bones. However, animal bones alone do not have sedative effects; traditionally used animal-based Chinese medicines, such as tiger or leopard bones, are known for strengthening muscles and bones. Why, then, do bones acquire sedative properties once fossilized? To date, the basis for *Os Draconis*'s sedative properties remains unclear. Therefore, any direct relationship between the radioactivity of the *Os Draconis* and their clinical efficacy requires further investigation.

Widely used today as a calming and tranquilizing medicine, the clinical demand for *Os Draconis* has been increasing. However, as *Os Draconis* fossils represent important geological relics with significant scientific value for understanding Earth's evolution and biological development, they are becoming increasingly scarce. Given the non-renewable nature of fossils and stringent national protection policies, the clinical supply of *Os Draconis* is tightening, leading to a proliferation of counterfeits. Heavily mineralized samples unsuitable for medicinal use are classified as fossilized *Os Draconis*, which are required to distinguished from authentic *Os Draconis*. These identification challenges highlight the need for objective methods beyond traditional macroscopic assessment, which often relies on features like bone structure, density, color, and the presence of characteristic surface markings known as "*Os Draconis* spots". These spots typically appear as localized black or dark brown stains or patches on the bone surface, generally understood to result from mineral staining or impregnation during the fossilization process.Therefore, rapid and accurate methods to distinguish authentic *Os Draconis* from counterfeit *Os Draconis* are urgently needed to ensure quality and clinical efficacy.

This study focused on the origins of *Os Draconis*, using methods such as literature review, radiocarbon dating (^{14}C), electron probe microanalysis (EPMA), polarizing light microscopy (PLM), X-ray diffraction (XRD), inductively coupled plasma mass spectrometry (ICP-MS), and Fourier-transform infrared spectroscopy (FTIR). We aim to outline more distinctive identification features for precise, economical authenticity testing of *Os Draconis*. EPMA and PLM were used for detailed observation of the microstructure, while XRD, ICP-MS, FTIR, and EPMA comprehensively analyzed *Os Draconis*'s components from macro to micro scales. We also conducted comparative studies on counterfeit products available on the market, fossilized *Os Draconis*, and lab-prepared samples from modern animal bones, observing micro-regional characteristics to distinguish authentic *Os Draconis* from counterfeits and lab-prepared samples, revealing unique microstructural features of *Os Draconis*.

Additionally, the study focused on porosity as a physical parameter, exploring the unique porosity of authentic *Os Draconis*, investigating its micro-performance in adsorption, and providing a scientifically sound explanation for this property.

Methods

Sample

A comprehensive collection of samples, categorized as authentic *Os Draconis*, fossilized *Os Draconis*, counterfeits, and lab-prepared modern animal bones, were procured from diverse sources. Detailed metadata for each sample, including specific procurement location, available information on geographical origin (primarily market location or labeled region of production), presumed/identified species category (e.g., mammalian fossil, modern bone), and macroscopic characteristics, are provided in Table 1. Voucher specimens are deposited at the Mineral Drug Identification Laboratory, Institute of Chinese Materia Medica, and China Academy of Chinese Medical Sciences.

It is important to note that for samples sourced from commercial TCM markets – which constitute the majority of our authentic *Os Draconis* and some of the fossilized *Os Draconis* samples – precise information regarding their original taphonomic history, specific burial environment, and detailed original geographical provenance (beyond the market of purchase or labeled region) is typically unavailable or unrecorded. Consequently, interpretations of elemental

Traditional Medicine Research 2026;11(3):18. http://doi.org/10.53388/TMR20250407002

Table 1 Information of samples

ID	Origin (province)	Date of process	Source	Dating results	Type of samples
1	Gansu	20191217-5	Hebei Anguo Medicinal Materials Market	> 43,500 BP	*Os Draconis*
2	Gansu	202206	Hebei Anguo Medicinal Materials Market	36,200 ± 310 BP	*Os Draconis*
3	Gansu	20161025	Lotus Pond Traditional Chinese Medicine Market	41,010 ± 470 BP	*Os Draconis*
4	Hebei	202203	Hebei Anguo Medicinal Materials Market	> 43,500 BP	*Os Draconis*
5	Henan	20180328	Tong Ren Tang (Dongsi Shitiao)	18,010 ± 50 BP	*Os Draconis*
6	Henan	94960102	Sunshine Pharmacy (Shizipo)	36,930 ± 290 BP	*Os Draconis*
7	Inner Mongolia	20191217-3	Hebei Anguo Medicinal Materials Market	> 43,500 BP	*Os Draconis*
8	Ningxia	20180305	Anhui Bozhou Medicinal Materials Market	> 43,500 BP	*Os Draconis*
9	Ningxia	20180305	Anhui Bozhou Medicinal Materials Market	> 43,500 BP	*Os Draconis*
10	Ningxia	18011802	Guoyaotang (Nongkesan)	33,000 ± 190 BP	*Os Draconis*
11	Ningxia	20191216	Hebei Anguo Medicinal Materials Market	> 43,500 BP	*Os Draconis*
12	Ningxia	202206	Hebei Anguo Medicinal Materials Market	43,140 ± 720 BP	*Os Draconis*
13	Ningxia	20161025	Lotus Pond Traditional Chinese Medicine Market	> 43,500 BP	*Os Draconis*
14	Ningxia	20191216	Hebei Anguo Medicinal Materials Market	> 43,500 BP	*Os Draconis*
15	Ningxia	20191216	Hebei Anguo Medicinal Materials Market	> 43,500 BP	*Os Draconis*
16	Ningxia	202206	Hebei Anguo Medicinal Materials Market	> 43,500 BP	*Os Draconis*
17	Ningxia	20161025	Lotus Pond Traditional Chinese Medicine Market	31,600 ± 170 BP	*Os Draconis*
18	Shanxi	190161061	Dongzhimen Hospital Affiliated to Beijing University of Chinese Medicine	> 43,500 BP	*Os Draconis*
19	Shanxi	202206	Anhui Bozhou Medicinal Materials Market	33,550 ± 230 BP	*Os Draconis*
20	Shanxi	202202	Hebei Anguo Medicinal Materials Market	42,120 ± 630 BP	*Os Draconis*
21	Shanxi	20191216	Hebei Anguo Medicinal Materials Market	39,960 ± 420 BP	*Os Draconis*
22	Shanxi	20161025	Lotus Pond Traditional Chinese Medicine Market	42,670 ± 580 BP	*Os Draconis*
23	Shanxi	202304	Hebei Anguo Medicinal Materials Market	35,980 ± 330 BP	*Os Draconis*
24	Shaanxi	202304	Hebei Anguo Medicinal Materials Market	35,730 ± 330 BP	*Os Draconis*
25	Hunan	202210	Anhui Bozhou Medicinal Materials Market	/	Fossified *Os Draconis*
26	Ningxia	202210	Anhui Bozhou Medicinal Materials Market	/	Fossified *Os Draconis*
27	Qinghai	202210	Anhui Bozhou Medicinal Materials Market	/	Fossified *Os Draconis*

Table 1 Information of samples (*continued*)

ID	Origin (province)	Date of process	Source	Dating results	Type of samples
28	Qinghai	202210	Anhui Bozhou Medicinal Materials Market	/	Fossified *Os Draconis*
29	Shandong	202210	Anhui Bozhou Medicinal Materials Market	/	Fossified *Os Draconis*
30	N/A	202304	Hebei Anguo Medicinal Materials Market	--	Counterfeit
31	N/A	202304	Hebei Anguo Medicinal Materials Market	--	Counterfeit
32	N/A	202304	Hebei Anguo Medicinal Materials Market	--	Counterfeit
33	Henan	17090903	Baikang Pharmacy (Gulou)	/	Counterfeit
34	Ningxia	20180305	Anhui Bozhou Medicinal Materials Market	/	Counterfeit
35	Ningxia	20191217	Hebei Anguo Medicinal Materials Market	/	Counterfeit
36	Ningxia	20161025	Sichuan Lotus Pond Traditional Chinese Medicine Market	/	Counterfeit
37	Ningxia	20161025	Sichuan Lotus Pond Traditional Chinese Medicine Market	/	Counterfeit
38	Ningxia	20161025	Sichuan Lotus Pond Traditional Chinese Medicine Market	/	Counterfeit
39	Shanxi	201610	Anhui Bozhou Medicinal Materials Market	/	Counterfeit
40	Shanxi	20161025	Sichuan Lotus Pond Traditional Chinese Medicine Market	/	Counterfeit
41	Shaanxi	201610	Anhui Bozhou Medicinal Materials Market	/	Counterfeit
42	Beijing Xianhui Supermarket	20230217	Cow dried at 40 °C	--	Fresh animal skeleton sample
43	Beijing Xianhui Supermarket	20230320	Cow calcination at 800 °C for 20 min	--	Fresh animal skeleton sample
44	Beijing Xianhui Supermarket	20230320	Cow calcination at 800 °C for 20 min	--	Fresh animal skeleton sample
45	Beijing Xianhui Supermarket	20230217	Cow boiling for 30 min, dried at 40 °C	--	Fresh animal skeleton sample
46	Beijing Xianhui Supermarket	20230320	Goat calcination at 800 °C for 20 min	--	Fresh animal skeleton sample
47	Beijing Xianhui Supermarket	20230217	Goat boiling for 30 min, dried at 40 °C	--	Fresh animal skeleton sample
48	Beijing Aoshikai Vegetable Market	20230217	Pig dried at 40 °C	--	Fresh animal skeleton sample
49	Beijing Aoshikai Vegetable Market	20201110	Pig boiling for 30 min, dried at 40 °C	--	Fresh animal skeleton sample
50	Beijing Aoshikai Vegetable Market	20230217	Pig boiling for 30 min, dried at 40 °C	--	Fresh animal skeleton sample

/ was counterfeit or suitable for ^{14}C test; -- was authentic samples and did not test.

variability linked to diagenesis for these market-sourced samples are made with this inherent limitation in mind, relying on general knowledge of bone diagenesis and comparative analysis with samples of more defined (e.g., lab-prepared) or broadly classifiable (e.g., counterfeit) origins.

To ensure the reliability and robustness of our findings, analyses were conducted on multiple distinct samples within each category (see Table 1 for the number of samples per category and their details).

Furthermore, experimental procedures incorporated technical replicates where appropriate and applicable for the specific analytical technique, as detailed in the subsequent sections, to account for analytical precision alongside inherent sample variability.

^{14}C dating

A total of 24 *Os Draconis* samples were selected for ^{14}C dating to investigate their chronological distribution and assess the age range of materials currently circulating in major TCM markets and pharmacies in China. These samples were specifically chosen to represent a range of key procurement locations and distribution points within the country, with detailed origins provided in Table 1. After removing visible impurities, approximately 2 grams of samples are taken for testing. As a critical verification step for these complex fossilized samples, we performed a two-point analysis on each of the 24 samples. This involved a pretreatment step to extract and isolate the organic collagen fraction. We then dated both the purified collagen and the inorganic bone apatite carbonate from the same sample. Comparing

the results from these two distinct components served as an internal consistency check to verify the reliability of the age determination for each sample and assess potential diagenetic contamination. An Accelerator-Based Mass Spectrometer (AMS, Model 250 Kev; National Electrostatics Corp., Middleton, WI, USA, with a precision of ± 0.001–0.004 fraction modern) was used to determine the ^{14}C content of both fractions. Concurrently, the stable carbon isotope ratio ($\delta^{13}C$) of the purified material (ideally collagen) was measured using an Isotope Ratio Mass Spectrometer (IRMS; Thermo Fisher Scientific, Waltham, MA, USA, with a precision of $\delta^{13}C$ ± −0.3‰). The raw ^{14}C age was then corrected for isotopic fractionation using these $\delta^{13}C$ values, normalizing to a standard $\delta^{13}C$ of −25‰ (PDB), to yield the final dating result for *Os Draconis*. Testing was conducted in accordance with ISO/IEC 17025:2017 standards.

PLM

For each prepared thin section, multiple fields of view were examined to identify and document representative microstructural features. A total of 24 authentic, 5 fossilized, 12 counterfeit, and 9 lab-prepared samples (as detailed in Table 1 and relevant results sections) were analyzed by Polarizing Light Microscope (PLM, Axio Scope.A1; Carl Zeiss, Oberkochen, Germany), using reflected light and a single polarization system for observation. Magnify the sample by 100 to 200 times to observe and analyze its detailed microstructural features. Use real-time depth of field extension technology to obtain color image data and mark areas that require further EPMA analysis.

EPMA

Electron scanning. According to the national standards including GB/T 4930-2008, GB/T 15074-2008, and GB/T 15617-2002, prepared thin sections are sprayed with carbon or gold powder on the surface to enhance sample conductivity. Secondary electron scanning is then performed for micro-area morphology analysis, and secondary electron images are captured. The standard samples were provided by the Institute of Mineral Resources, Chinese Academy of Geological Sciences, including apatite (K26 GSB 01-1478-2001), silicon dioxide (GSB A70068-92), basaltic glass, and others. The electron probe X-ray micro-analyzer used was manufactured by Electron Probe Micro-Analyzer (EPMA, Model EPMA-1720H; Shimadzu Corporation, Kyoto, Japan).

EPMA analysis. Specific micro-area regions were selected for electron probe compositional analysis based on polarized light microscope characteristics of the sample. Backscattered electron scanning was performed, and typical locations in the backscattered images were selected for electron probe element analysis to determine elemental composition, identifying primary research targets for each sample area. For each target mineral phase or feature within a sample, 2–3 distinct micro-areas were selected for quantitative analysis (technical replicates). Across all sample categories, EPMA quantitative analysis was performed on a total of 262 points selected from 24 authentic *Os Draconis* samples, 5 fossilized *Os Draconis* samples, 12 counterfeit samples, and 9 lab-prepared modern animal bone samples (biological replicates, as listed in results). For each target mineral phase or feature identified within a single sample, 2–3 distinct micro-areas were selected for quantitative analysis to serve as technical replicates, assessing local compositional homogeneity. By measuring the elemental composition and mass fraction in these micro-areas, mineral types were further clarified. Systematic mineralogical indices determined the main mineral element composition of each point, leading to the calculation of the primary mineral phase for each sample. The electron probe X-ray micro-analyzer used was a Electron Probe Micro-Analyzer (EPMA, Model EPMA-1720H; Shimadzu Corporation, Kyoto, Japan). Analysis conditions were accelerating voltage 15.0 kV, beam current 50.0 nA, and spot size 5 μm. To resolve potentially overlapping mineral phases, such as hydroxyapatite and calcite, in regions with mixed signals, EPMA analysis relied on several key strategies. Primarily, the presence or absence of phosphorus (P) was a critical discriminator, as hydroxyapatite is rich in P while calcite ($CaCO_3$) is not. Quantitative elemental analysis provided stoichiometric data, allowing comparison with ideal mineral compositions. Additionally, backscattered electron imaging, sensitive to average atomic number, often revealed distinct grey levels for different mineral phases, guiding the selection of homogenous areas for point analysis. The high spatial resolution of EPMA (5 μm spot size) further facilitated the analysis of discrete mineral grains if they were larger than the interaction volume. Observations from polarized light microscopy, noting differences in optical properties between apatite and calcite, also informed the selection of target areas for EPMA to minimize analysis of overtly mixed regions.

XRD

For testing samples, impurities were removed, samples were crushed and sieved to 200 mesh. A scraper was used to collect the black-brown to black powder of *Os Draconis* for bone spot testing, and yellowish soil impurities were collected for soil testing. A single, high-quality XRD scan was performed for each of the 45 prepared powder samples, the number of distinct samples analyzed per category (biological replicates) is detailed in results While technical replicates (multiple scans of the same powder) were not performed, which is standard for phase identification, Reliability of phase identification was ensured through rigorous full-spectrum fitting and comparison against standard patterns in the international PDF database using EVA (Bruker AXS, Billerica, MA, USA) and Jade 6 (International Centre for Diffraction Data, Newtown Square, PA, USA) software. The number of distinct samples analyzed per category is detailed in results . The differentiation of overlapping mineral phases such as hydroxyapatite and calcite by XRD was primarily based on their unique crystal structures, which result in distinct sets of characteristic diffraction peak positions (2θ angles) and relative intensities. Even with some peak overlap, the full-spectrum fitting routines in the analysis software (e.g., EVA, and as further processed in MID Jade6), when compared against standard patterns in the international PDF database, could effectively identify and distinguish the constituent phases present in the mixture by considering the entire diffraction pattern. The single-crystal X-ray diffractometer used was the D8 Advance by Bruker. Software used included MID Jade6 for analysis and Origin 2022 (OriginLab Corporation, Northampton, MA, USA) for data analysis and plotting.

ICP-MS

Reagent. 65% Nitric Acid was purchased from Xilong Scientific Co., Ltd., Shantou, China, 2311207, superior grade; Hydrofluoric Acid was purchased from Xilong, 231112, superior grade; 30% Hydrogen Peroxide was purchased from Xilong, 231114, superior grade. Standard solutions for elements Zr, Zn, Yb, W, V, Tm, Tl, Ti, Te, Tb, Ta, Sr, Sn, Sm, Si, Se, Sc, Sb, S, Ru, Rh, Pt, Pr, Pd, Pb, P, Ni, Nd, Nb, Na, Mo, Mn, Mg, Lu, Li, La, K, Ir, In, Ho, Hg, Hf, Ge, Gd, Ga, Fe, Eu, Er, Dy, Cu, Cr, Co, Ce, Cd, Ca, Bi, Be, Ba, B, Au, As, Al, Ag were purchased from National Institute of Metrology, Beijing, China Testing & Certification Co., Ltd.

Experimental methods. After impurity removal, approximately 0.1 g of each sample was weighed and prepared according to China National Standard GB/T 14506.28-2010. About 6 mL of nitric acid, 1 mL of hydrofluoric acid, 1 mL of hydrochloric acid, and 1 mL of hydrogen peroxide were added, heated to 190 ˚C for 8 h, then cooled, transferred, volume adjusted, diluted, and tested for element content. Measurement conditions (Agilent 7700) : Argon pressure: 0.60 MPa, Helium pressure: 0.15 MPa, Cooling air flow rate: 14.0 L/min, Auxiliary air flow rate: 0.80 L/min, Nebulizer flow rate: 1.05 L/min, RF power: 1,550 W, Nebulizer chamber temperature: 2.5 ˚C, Pump speed: 40 rpm, Sampling depth: 5.0 mm, Scan repetitions: 30, Data collection mode: KED. Each prepared sample solution underwent instrumental analysis three times (technical replicates) to ensure measurement precision, and the average reading was used for subsequent calculations. ICP-MS analysis was performed on a total of 8 authentic *Os Draconis* samples, 5 fossilized *Os Draconis* samples, 4 counterfeit samples, and 5 lab-prepared modern animal bone samples (as detailed in results). Each final prepared sample solution underwent

instrumental analysis three times (technical replicates) to ensure measurement precision, and the average value was used for subsequent calculations. The final content of each element in the sample = instrument reading × dilution factor × volume/sample mass.

Mercury intrusion porosimetry

A single mercury intrusion analysis was conducted on one prepared piece from each of the 21 selected representative samples (7 authentic *Os Draconis*, 5 fossilized *Os Draconis*, 4 counterfeit, and 5 lab-prepared samples, as detailed in results . While technical replicates on the same prepared piece were not performed due to the destructive nature of the analysis, the analysis of multiple distinct samples across the different categories (biological replicates) provides data on the range and variability of porosimetric parameters within each group. After removing surface impurities from each sample, they were cut into pieces smaller than 1 cm, washed three times with pure water, and dried in a 60 °C oven for 4 h. Once cooled, each sample was weighed, placed into a 3 mL dilatometer, and sealed with vacuum grease. After sealing, each sample was weighed again. The sample tube was then placed in a low-pressure station for analysis, with the low-pressure process ending when the pressure reached 0.2 MPa. At this point, mercury filled the dilatometer and the macropores within the sample. The dilatometer was removed from the low-pressure chamber for the next weighing step. It was then placed in a high-pressure station for high-pressure analysis, where increasing pressure forced mercury into the sample's micropores. After reaching 200 MPa, the pressure was reduced to atmospheric pressure, completing the mercury removal process. This procedure provided measurements of total pore area, pore size, porosity, density, and other physical parameters. The analysis was conducted using an automated mercury intrusion porosimeter, AutoPore V (Micromeritics Instrument Corporation, Shanghai, China), equipped with two low-pressure chambers and one high-pressure chamber, and using a 3 mL solid dilatometer. Analysis followed the Standards: ISO 15901-1 and GB/T 21560.1-2008.

FTIR

The experiment uses pure hydroxyapatite reagent (HAP, Macklin, $Ca_{10}(OH)_2(PO_4)_6$, CAS: 12167-74-7, 34–40% Ca) as a control sample. FTIR analysis was conducted on a total of 8 authentic *Os Draconis*, 5 fossilized *Os Draconis*, 7 counterfeit, and 4 lab-prepared modern animal bone samples (biological replicates, as listed in this section). The powders were then sifted through a 200-mesh sieve and tested in ATR mode. The FTIR measurement range was set from 4,000 cm^{-1} to 400 cm^{-1}, with 16 instrument scans averaged to produce each final spectrum for a given sample, enhancing the signal-to-noise ratio (instrumental replication). The resulting infrared spectra were processed by automatic baseline correction and y-axis normalization. Fourier Transform Infrared Spectrometer was from Perkin Elmer, USA. Data analysis and plotting software was Origin2022 (OriginLab Corporation, Northampton, MA, USA).

Statistical analysis

Quantitative data are presented as mean ± standard deviation (SD) or median (interquartile range) as appropriate, depending on data distribution. To assess significant differences in quantitative parameters (e.g., Ca/P ratios, elemental concentrations, porosity metrics) among the four main groups (authentic *Os Draconis*, fossilized *Os Draconis*, counterfeit, and lab-prepared samples), one-way analysis of variance (ANOVA) was performed, followed by post-hoc tests (e.g., Tukey's HSD or Dunnett's test, depending on comparisons) for pairwise comparisons if the overall ANOVA was significant. For data not meeting ANOVA assumptions (e.g., normality, homogeneity of variances, assessed by Shapiro-Wilk and Levene's test, respectively), non-parametric equivalent tests such as the Kruskal-Wallis test followed by Dunn's test for pairwise comparisons were used. A *P*-value < 0.05 was considered statistically significant. All statistical analyses were performed using Prism version 10 (GraphPad Software, Boston, MA, USA).

Results

Physical characteristics of samples

A total of 50 sample batches were collected and prepared for this study (Table 1). Samples numbered 1 to 41 were purchased between 2016 and 2023 from herb markets, pharmacies, and hospitals. Samples 42 to 50 (9 batches) were lab-prepared using modern animal bones to simulate contemporary counterfeits; these samples were derived from the easily available tibias of modern animals such as cows, goat, and pigs and were prepared by calcining, boiling, and low-temperature drying. All samples were authenticated by Researcher Zhijie Zhang from the Institute of Chinese Materia Medica, China Academy of Chinese Medical Sciences. According to the standard that *Os Draconis* is recognized as authentic only if it dates back over ten thousand years, 24 batches were classified as authentic *Os Draconis*, while 12 batches were identified as counterfeit (9 were labeled counterfeit due to inconsistent carbonate results from two sampling points, and 3 were declared counterfeit at the point of sale) [22]. Five batches were classified as fossilized *Os Draconis* based on signs of mineralization.

Animal bones are categorized into cranial, trunk, and limb bones, and can be further classified into long, short, flat, and irregular bones. *Os Draconis* used for medicinal purposes generally consists of fragmented fossilized bones with no archaeological value. Market samples typically include limb bone fragments, such as pieces from the humerus, radius, ulna, femur, tibia, and fibula. Long bones are composed of a shaft and epiphyses, containing compact bone, spongy bone, periosteum, articular cartilage, and marrow. Compact bone covers the shaft and epiphyses' outer surface, and includes lamellae, osteons (central canal and osteon lamellae), and interstitial lamellae; spongy bone, found in the epiphyses and shaft's marrow cavity surface, forms a trabecular network of bone plates and cells resembling a sponge structure.

Observations of the 24 batches identified as authentic *Os Draconis* via ^{14}C dating reveal that they retain the external morphology of animal bones, appearing in bone-like or irregularly fragmented forms of varying sizes, generally white or off-white in color. The compact bone is slightly dense and relatively smooth, with some samples showing cracks or striations, and others displaying black or dark brown stains (*Os Draconis* spots) due to staining. The spongy bone often has a honeycomb structure, sometimes filled with soil or minerals (Figure 1A–1H). It has strong hygroscopic properties, no odor, and no taste.

Fossilized *Os Draconis* mostly retains the external shape of animal bones, often in large pieces that are bone-like in appearance, with a gray-yellow, brown-yellow, or brown-gray hue, filled with mineral deposits. The compact bone is dense and solid, with large dark stains in brownish-yellow or reddish-brown hues on some surfaces, and black or dark brown stains on others due to impregnation. The spongy bone's honeycomb structure is often filled with minerals (Figure 1I–1Q). It is heavy, solid, and difficult to break, with strong hygroscopicity, which has no odor, and no taste.

Counterfeit samples vary in shape, often irregular, with some displaying a bone-like appearance but with smaller diameters. They are generally pale, milky white, or grayish-white. The surface of the compact bone shows no *Os Draconis* spots. The honeycomb structure of the spongy bone is visible and unfilled. Some samples lack a clear distinction between compact and spongy bone, with a smooth surface and sharp edges (Figure 2A–2C). They are solid or light, with some being brittle and easily crumbling with white dust falling off when touched. They exhibit hygroscopic properties, a slight odor, and a mild taste.

To simulate counterfeit *Os Draconis* made from modern animal bones, the experiment used tibias from cows, goat, and pigs, preparing 9 batches using low-temperature drying, boiling, and calcination methods. These samples retain the physical characteristics of animal bones (Figure 2D–2K). Low-temperature dried samples have intact shapes with a pale yellow surface, keratin-like compact bone, tough

texture, and a noticeable oily sheen. Boiled samples also have intact shapes with a yellow-white surface, no cracks, and a hard texture, with an oily sheen visible. Calcined samples are mostly broken into fragments, with a gray-white surface, cracks, light weight, and brittleness, without an oily sheen. Boiled and low-temperature dried samples have a distinct greasy odor, while calcined samples have a faint odor and mild taste.

Characteristics of authentic *Os Draconis*

Based on the microscopic characteristics of ultrastructure observed under polarized light microscopy, 24 batches of samples generally retain the microstructural features of animal bone, with slight morphological differences possibly due to variations in animal species. Under polarized light microscopy, the dense bone in authentic samples consists of closely packed osteons, which are circular or irregularly shaped with a Haversian canal in the center. The osteonal lamellae appear as ring-like structures with numerous osteocyte lacunae, arranged differently depending on the shape of the osteons and Haversian canals, mostly ring-like. Irregular interstitial lamellae fill the space between osteons. Across the entire cross-section, deformed osteons are visible, often intersected by multiple cracks extending into or through the osteons. Osteons that are penetrated by cracks often show deformation, displacement, or fracture (Figure 3A–3D). These cracks, which can penetrate osteons, are a distinguishing feature of authentic *Os Draconis*.

EPMA offers nanoscale morphology analysis capability. Secondary

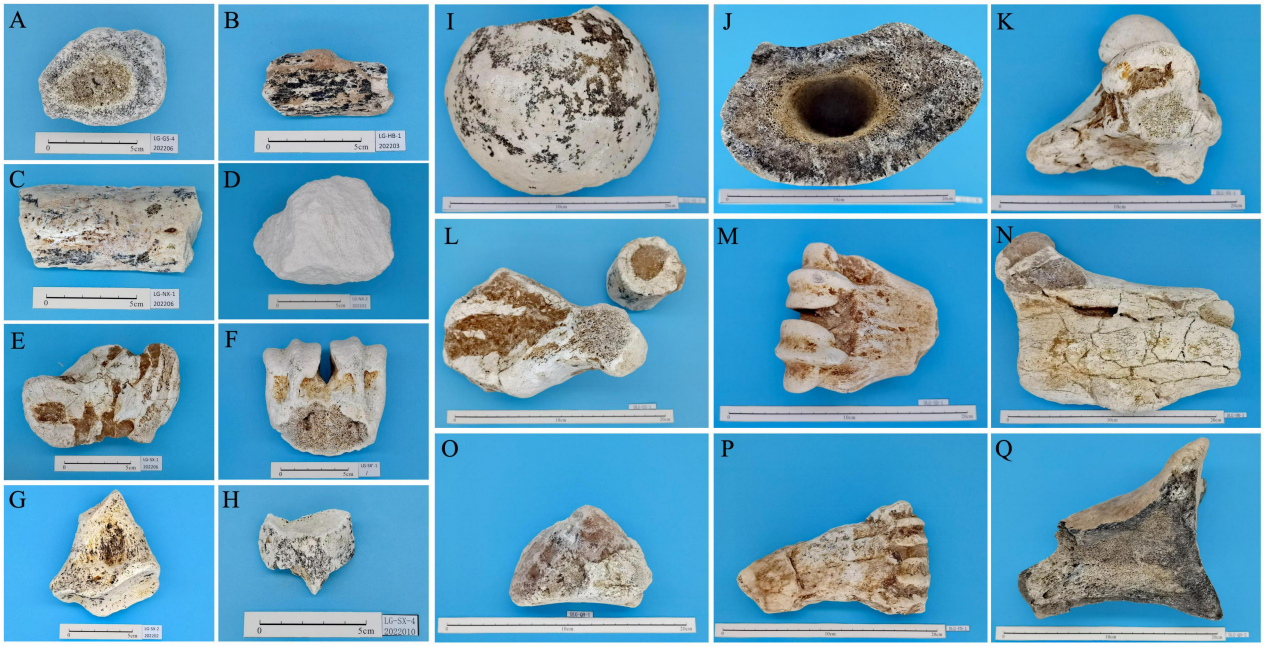

Figure 1 Characteristics of authentic *Os Draconis* and fossilized *Os Draconis*. (A–H) authentic *Os Draconis*; (I–Q) fossilized *Os Draconis*.

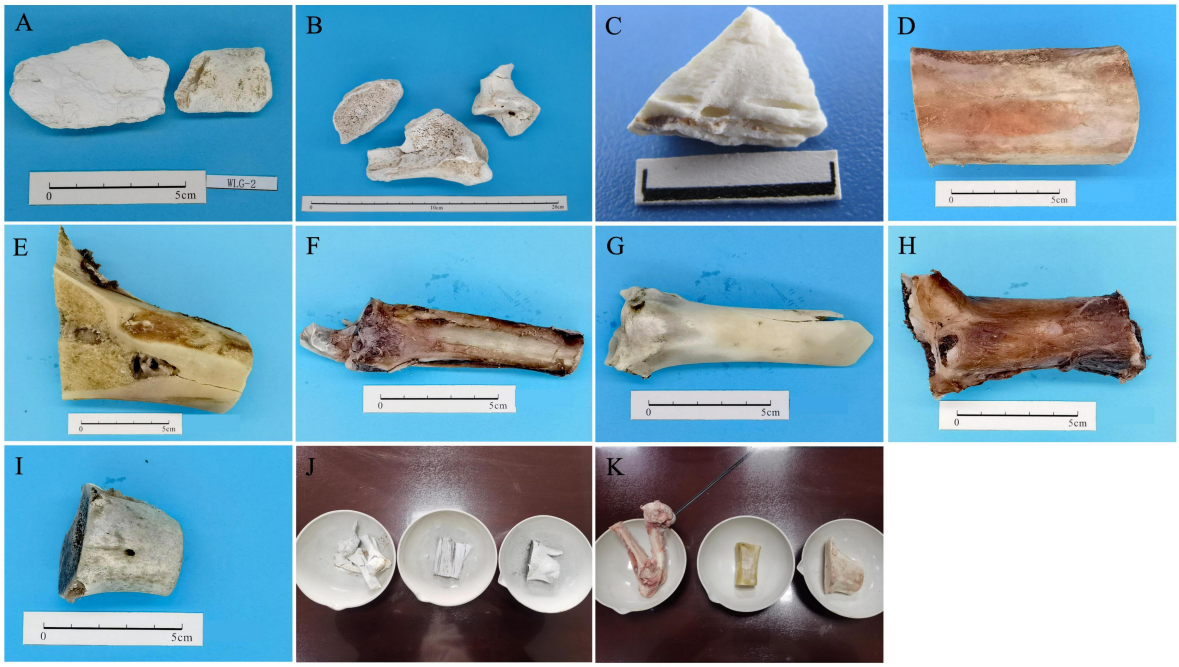

Figure 2 Characteristics of counterfeit *Os Draconis* and lab-prepared samples. (A–C) counterfeit *Os Draconis*; (D–K) lab-prepared samples.

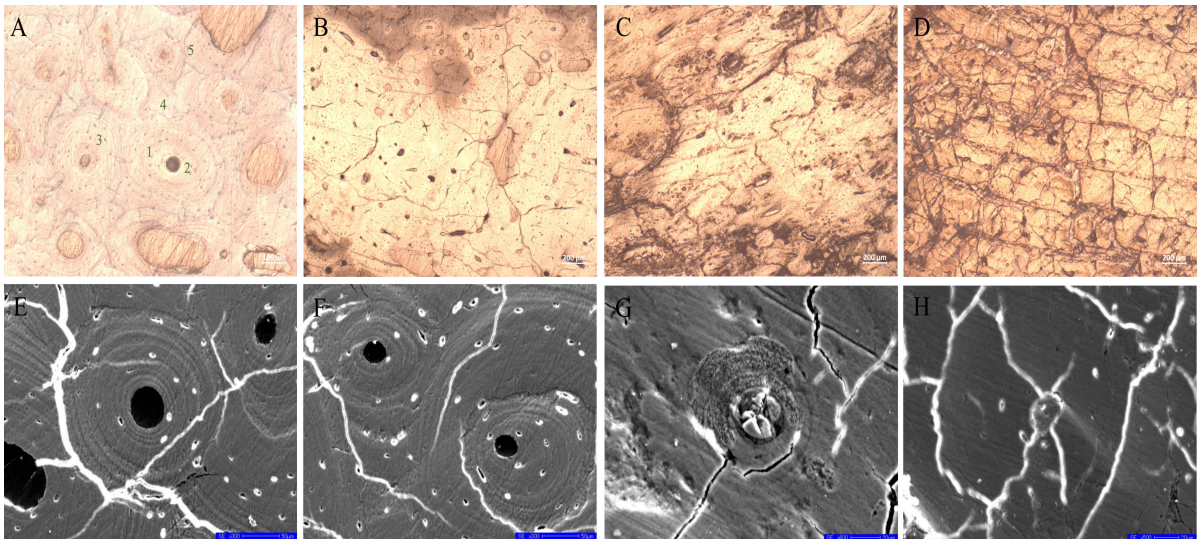

Figure 3 Characteristics of authentic *Os Draconis*. (A–D) polarized light microscopy image, for A, 1: Osteon, 2: Haversian canal, 3: Lacuna, 4: Interstitial lamellae, 5: Cleft. Scale bar = 200 μm. (E–H) Secondary electron probe image of a cross-section of compact bone. Scale bar = 50 μm.

electron images, reflecting surface features around 10 nm, can provide additional ultrastructural information about the sample. The secondary electron images of a cross-section (Figure 3E–3H) show that dense bone contains circular or irregularly shaped osteons. The Haversian canals within osteons are mostly circular, some centrally located, some offset, and some appear hollow or filled. Irregular interstitial lamellae fill the spaces between osteons. Surrounding the Haversian canals, there are 5 to 20 layers of concentric lamellae with irregular arrangements and numerous oval-shaped lacunae representing osteocyte spaces. The outlines (cement lines) of osteons are clear, with many visible and distinct cracks extending into or through them.

XRD analysis (Figure 4A, Table 2) reveals that hydroxyapatite mineral phases were detected in all 29 samples, with five samples identified as synthetic hydroxyapatite. Ten samples also showed calcium carbonate calcite mineral phases, and eight samples contained quartz. Careful scraping of black-brown to black areas (spot area) from 11 batches of samples revealed through XRD that these sections contained calcite with magnesium and quartz, unlike the whitish bone-like substance (Table 3). Spot area is believe to be essential part of *Os Draconis*. The soil-impurity-containing portions included hydroxyapatite, as well as calcium carbonate, quartz, magnesium calcite, muscovite, octahedrite, dolomite, and montmorillonite (Table 4).

ICP-MS elemental analysis of eight authentic samples yielded results (Table 5) and standard curves for Al, As, Ba, Ca, Cr, Fe, K, Mg, Na, P, Si, and Sr elements (Figure 4A). The average Ca/P ratio for samples was 2.23. After normalizing the rare earth element data against primitive mantle values (Figure 4B, 4C), we observed significant enrichment of La, Eu, Er, and Lu and marked depletion of Sc in genuine keel samples, with slight depletion in other elements. This is likely related to the burial environment and fossilization process.

To investigate the elemental composition and mineral phase differences in *Os Draconis* and other samples, we performed EPMA mineral phase analysis on 24 authentic samples, including 10 samples of dense bone and 14 of cancellous bone. Based on the principle of selecting different mineral phases in the same field of view, 262 points were selected, identifying 13 mineral phases: 210 points for hydroxyapatite, 27 for calcium carbonate calcite, 6 for quartz, 1 for cavity, and other points containing minerals like dolomite, chlorite, albite, and plagioclase with elements Al, Mg, Fe, Ba, Cr, Na, and K (Table 6). Hydroxyapatite was found in 80.15% of the bone lamellae, making it the primary mineral phase. Secondary filler minerals, mainly calcite and quartz, were distributed in dense bone Haversian canals, cancellous bone cavities, and cracks. For calcite mineral phases, 27 points were detected: 15 in cancellous bone, 6 in Haversian canals, and 6 in cracks; for quartz mineral phases, 6 points were identified, 4 in cancellous bone cavities and 2 in dense bone Haversian canals. Three points were identified as dolomite, three as chlorite, one as albite, one as plagioclase, and one as a cavity. Figure 4D and Supplementary Table S1 show three points in dense bone: point 1 in the lacuna, point 2 in the lamellae, and point 3 in the Haversian canal. Points 1 and 2 were hydroxyapatite, and point 3 was calcite. Figure 4E and Supplementary Table S2 show points 1, 2, and 3 in dense bone Haversian canals and points 4–11 in lamellae. Point 1 was quartz, while other points were hydroxyapatite.

To further investigate the mineral phase differences in various parts of the keel, quantitative EPMA analysis was conducted on 24 samples. The normal calcium-phosphorus ratio in modern skeletal bone is around 2:1. From 208 points identified as hydroxyapatite, the Ca/P ratio was calculated. The average Ca/P value for all samples was 2.92.

Characteristics of fossilized, counterfeit *Os Draconis* and lab-prepared *Os Draconis*

Microscope of fossilized, counterfeit *Os Draconis* and lab-prepared *Os Draconis*. The over-fossilized *Os Draconis*, referred as fossilized *Os Draconis* in the following content, still shows the structure of bone units, but these units are more compact or fused together. Haversian canals are filled, and fractures and compressive deformation are more evident. Under polarized microscopy, the dense bone consists of tightly arranged bone units in round, square, or polygonal shapes; Haversian canals are mostly filled with minerals of low relief; some bone lacunae and cement lines are indistinct (Figure 5A). The secondary electron images from electron probe analysis reveal irregular shapes of bone units in the dense bone. Some Haversian canals are filled and deformed, while others are compressed to dot-like forms; bone lamellae surrounding Haversian canals are fused with indistinct layers, and bone lacunae are irregularly arranged. Fractures running through bone units are more common (Figure 5B).

Counterfeit samples show varied ultrastructures. In samples with bone morphology, bone units are regular and orderly without fractures running through them. Polarized microscopy shows tightly arranged round-shaped bone units in the dense bone, with Haversian canals usually at the center of the bone units, and distinct cement lines (Figure 5C). Some samples lack the characteristic bone unit structure (Figure 5D). Secondary electron images of samples with bone morphology reveal regular shapes of dense bone units, with Haversian canals at the center of bone units; bone lacunae surround the Haversian canals, and no lamellar structure is visible. Fractures occur along cement lines, with no fractures through bone units (Figure 5E).

Traditional Medicine Research 2026;11(3):18. http://doi.org/10.53388/TMR20250407002

Table 2 XRD of authentic *Os Draconis*

ID	Name	Hydroxyapatite	Synthetic hydroxyapatite	Calcium carbonate calcite mineral phases	Quartz
1	LG-GS-1	√	/	/	/
2	LG-GS-2	√	/	√	√
3	LG-GS-3	/	√	√	√
4	LG-GS-4 (2#)	√	/	√	/
5	LG-GS-5	√	/	/	/
6	LG-GS-6	√	/	/	/
7	LG-GS-7	√	/	√	/
8	LG-HB-1 (4#)	√	/	/	/
9	LG-HB-2	√	/	/	/
10	LG-HB-3	/	√	/	/
11	LG-HN-1	√	/	/	/
12	LG-HN-2	√	/	/	√
13	LG-NM-1	/	√	√	/
14	LG-NM-2	√	/	√	/
15	LG-NM-3	√	/	√	/
16	LG-NX-1 (16#)	√	/	/	/
17	LG-NX-2	√	/	/	/
18	LG-NX-3	√	/	/	/
19	LG-NX-4	/	√	/	√
20	LG-NX-5	√	/	√	√
21	LG-NX-6	√	/	/	/
22	LG-SHX-1 (24#)	√	/	/	/
23	LG-SHX-2	√	/	/	/
24	LG-SHX-3	√	/	/	/
25	LG-SX-1	/	√	√	√
26	LG-SX-2 (20#)	√	/	/	√
27	LG-SX-3 (23#)	√	/	/	/
28	LG-SX-4	√	/	/	/
29	LG-SX-5	√	/	√	√

XRD, X-ray diffraction.

Table 3 XRD of authentic *Os Draconis* (spot area)

ID	Name	Hydroxyapatite	Synthetic hydroxyapatite	Calcium carbonate calcite mineral phases	Quartz	Calcite with magnesium
1	LG-GS-1-white	√	/	/	/	/
	LG-GS-1-black	√	/	/	/	√
2	LG-GS-4-white	√	/	√	/	/
	LG-GS-4-black	√	/	/	√	√
3	LG-HB-1-white	√	/	/	/	/
	LG-HB-1-black	√	/	/	√	√
4	LG-HB-2-white	√	/	/	/	/
	LG-HB-2-black	√	/	/	√	/
5	LG-HB-3-white	/	√	/	/	/
	LG-HB-3-black	√	/	/	√	/
6	LG-HN-1white	√	/	/	/	/
	LG-HN-1-black	√	/	/	√	/
7	LG-NX-4-white	/	√	/	√	/
	LG-NX-4-black	√	/	/	/	/

Table 3 XRD of authentic *Os Draconis* (spot area) (*continued*)

ID	Name	Hydroxyapatite	Synthetic hydroxyapatite	Calcium carbonate calcite mineral phases	Quartz	Calcite with magnesium
8	LG-SHX-3-white	√	/	/	/	/
	LG-SHX-3-black	√	/	/	√	√
9	LG-SX-2-white	√	/	/	√	/
	LG-SX-2-black	√	/	/	√	/
10	LG-SX-3-white	√	/	/	/	/
	LG-SX-3-black	√	/	/	/	√
11	LG-SX-4-white	√	/	/	/	/
	LG-SX-4-black	√	/	/	√	√

White was from *Os Draconis*, Black was from spot area of the same sample. XRD, X-ray diffraction.

Table 4 XRD of authentic *Os Draconis* (soil-impurity)

ID	Name	Hydroxyapatite	Calcium carbonate	Quartz	Calcite with magnesium	muscovite	Octahedrite	Dolomite	Montmorillonite
1	LG-HB-1-white	√	/	/	/	/	/	/	/
	LG-HB-1yellow	/	/	√	√	√	√	/	/
2	LG-NX-4-white	√	/	√	/	/	/	/	/
	LG-NX-4-yellow	√	√	√	/	/	/	√	√
3	LG-SHX-1-white	√	/	/	/	/	/	/	/
	LG-SHX-1-yellow	√	/	√	/	/	/	/	/
4	LG-SX-1-white	√	√	√	/	/	/	/	/
	LG-SX-1-yellow	√	√	√	/	/	/	/	√
5	LG-SX-2-white	√	/	√	/	/	/	/	/
	LG-SX-2-yellow	√	/	√	/	/	/	/	/

XRD, X-ray diffraction.

Table 5 ICP-MS of authentic *Os Draconis*

Atomic number	Element	Concentration (mg/kg)							
		2#	4#	12#	16#	19#	20#	23#	24#
3	Li	0.586	0.751	0.229	0.209	0.361	0.677	0.564	0.428
4	Be	0.418	0.522	0.089	0.589	0.501	0.696	0.242	0.507
5	B	14.773	0.296	584.697	0.103	0.277	29.937	18.872	27.546
11	Na	4,093.186	4,453.537	8,885.586	3,656.289	2,710.491	3,642.720	3,436.166	5,381.787
12	Mg	1,584.107	1,326.076	1,209.850	1,678.978	1,476.731	1,248.264	1,094.750	1,784.092
13	Al	361.955	301.525	285.903	367.725	1560.760	226.478	33.910	195.201
14	Si	246.753	183.728	152.279	308.482	481.150	338.629	54.693	345.128
15	P	144,321.331	150,728.839	126,851.351	146,224.319	122,283.747	146,404.919	160,355.045	141,177.690
16	S	823.988	1,144.359	16,485.811	688.564	600.838	727.030	1,552.270	1,457.071
19	K	292.012	237.027	153.638	222.210	922.578	138.047	55.768	166.730
20	Ca	325,603.920	331,457.074	290,400.400	326,063.941	292,114.325	322,250.734	328,374.690	315,064.166
21	Sc	0.437	0.831	0.337	0.127	0.540	0.412	0.060	0.773
22	Ti	24.138	35.714	0.253	0.608	43.198	12.051	0.596	0.745
23	V	15.775	9.352	0.241	0.787	0.565	10.825	0.683	0.590
24	Cr	8.111	13.976	0.628	10.175	19.387	0.772	11.606	0.747
25	Mn	75.305	9.845	392.332	0.519	35.284	387.882	14.839	0.813
26	Fe	289.417	374.634	145.464	155.090	1,374.805	218.182	97.075	142.085
27	Co	0.254	0.252	0.187	0.299	0.256	0.324	0.227	0.190
28	Ni	0.284	0.573	0.306	0.201	0.409	0.207	0.245	0.540
29	Cu	0.549	32.647	0.624	0.493	19.317	0.665	2.340	0.427
30	Zn	76.681	75.932	38.859	43.172	80.612	75.769	67.007	38.543

Table 5 ICP-MS of authentic *Os Draconis* (*continued*)

Atomic number	Element	Concentration (mg/kg)							
		2#	4#	12#	16#	19#	20#	23#	24#
31	Ga	0.752	0.329	6.022	0.638	0.321	0.370	0.452	0.430
32	Ge	0.590	0.751	0.598	0.695	0.675	0.685	0.555	0.508
33	As	0.381	0.783	0.303	30.691	0.741	11.063	0.207	21.086
34	Se	0.589	0.573	0.568	0.744	0.471	0.664	0.405	0.748
38	Sr	1,400.964	1,461.847	1,891.867	1,706.549	675.618	1,161.410	469.355	1,936.666
40	Zr	0.702	38.714	0.279	0.805	0.749	88.788	0.441	35.661
41	Nb	0.372	0.785	0.641	0.637	0.708	10.695	0.470	0.492
42	Mo	0.336	0.467	0.098	0.397	0.265	0.255	0.164	0.439
44	Ru	0.487	0.390	0.415	0.640	0.395	0.502	0.586	0.511
45	Rh	0.388	0.567	0.513	0.488	0.560	0.674	0.425	0.671
46	Pd	0.425	0.510	0.534	0.304	0.303	0.320	0.487	0.356
47	Ag	27.411	0.243	0.514	0.444	0.424	1598.153	0.444	0.804
48	Cd	0.118	0.425	0.034	0.023	0.271	0.058	0.075	0.072
49	In	0.504	0.234	0.789	0.426	0.549	11.536	0.334	0.717
50	Sn	0.549	0.704	0.428	0.615	0.250	0.670	0.483	0.268
51	Sb	0.280	0.278	0.188	0.238	0.219	0.140	0.393	0.259
52	Te	0.431	0.682	0.821	0.286	0.437	10.961	0.399	0.384
56	Ba	372.138	417.334	145.013	323.960	291.940	490.499	143.969	375.508
57	La	22.332	34.230	15.025	0.705	13.182	0.540	0.408	47.438
58	Ce	0.469	0.239	0.339	0.244	0.301	0.267	0.292	0.327
59	Pr	0.207	0.156	0.544	0.501	0.269	0.278	0.147	0.366
60	Nd	0.773	0.323	0.253	0.697	0.710	0.559	0.298	0.464
62	Sm	0.265	0.125	0.136	0.199	0.106	0.328	0.202	0.443
63	Eu	0.606	0.848	0.611	0.710	0.626	0.790	0.471	0.619
64	Gd	0.703	8.737	0.380	0.496	0.390	0.482	0.264	0.481
65	Tb	0.064	0.167	0.111	0.147	0.203	0.234	0.038	0.502
66	Dy	0.295	0.635	0.324	0.244	0.285	0.206	0.220	0.511
67	Ho	0.145	0.110	0.023	0.010	0.031	0.060	0.026	0.130
68	Er	0.663	0.571	0.455	0.754	0.708	4.073	0.509	0.535
69	Tm	0.056	0.101	0.053	0.016	0.025	0.184	0.054	0.154
70	Yb	0.161	0.401	0.211	0.176	0.324	0.353	0.089	0.315
71	Lu	0.276	0.295	0.265	0.277	0.252	0.267	0.251	0.300
72	Hf	0.466	0.666	0.686	0.460	0.470	0.319	0.537	0.596
73	Ta	0.203	0.400	0.479	0.541	0.530	0.486	0.210	0.636
74	W	0.277	0.294	0.273	0.224	0.236	0.201	0.288	0.199
77	Ir	0.515	0.443	0.275	0.393	0.508	0.458	0.539	0.267
78	Pt	0.358	0.244	0.341	0.538	0.277	0.604	0.246	0.380
79	Au	0.354	0.770	0.437	1.059	0.367	0.657	0.428	0.279
80	Hg	0.409	0.429	0.281	0.258	0.226	0.586	0.565	0.313
81	Tl	0.258	0.253	0.541	0.526	0.500	0.382	0.198	0.283
82	Pb	0.728	22.638	0.811	8.862	0.479	9.201	0.523	0.450
83	Bi	0.257	0.279	0.312	0.348	0.264	0.517	0.228	0.297

ICP-MS, inductively coupled plasma mass spectrometry.

Traditional Medicine Research 2026;11(3):18. http://doi.org/10.53388/TMR20250407002

Table 6 Analysis of authentic *Os Draconis* (mineral phase)

Mineral phase	Count	Percentage
Hydroxyapatite	210	80.15%
Calcium carbonate calcite	27	10.31%
Quartz	6	2.29%
Ba	3	1.15%
Cr	3	1.15%
Dolomite	3	1.15%
Chlorite	3	1.15%
Al	2	0.76%
Fek, Ba, Ca	1	0.38%
Fe, Ba, Mg	1	0.38%
Cavity	1	0.38%
Albite	1	0.38%
Plagioclase	1	0.38%

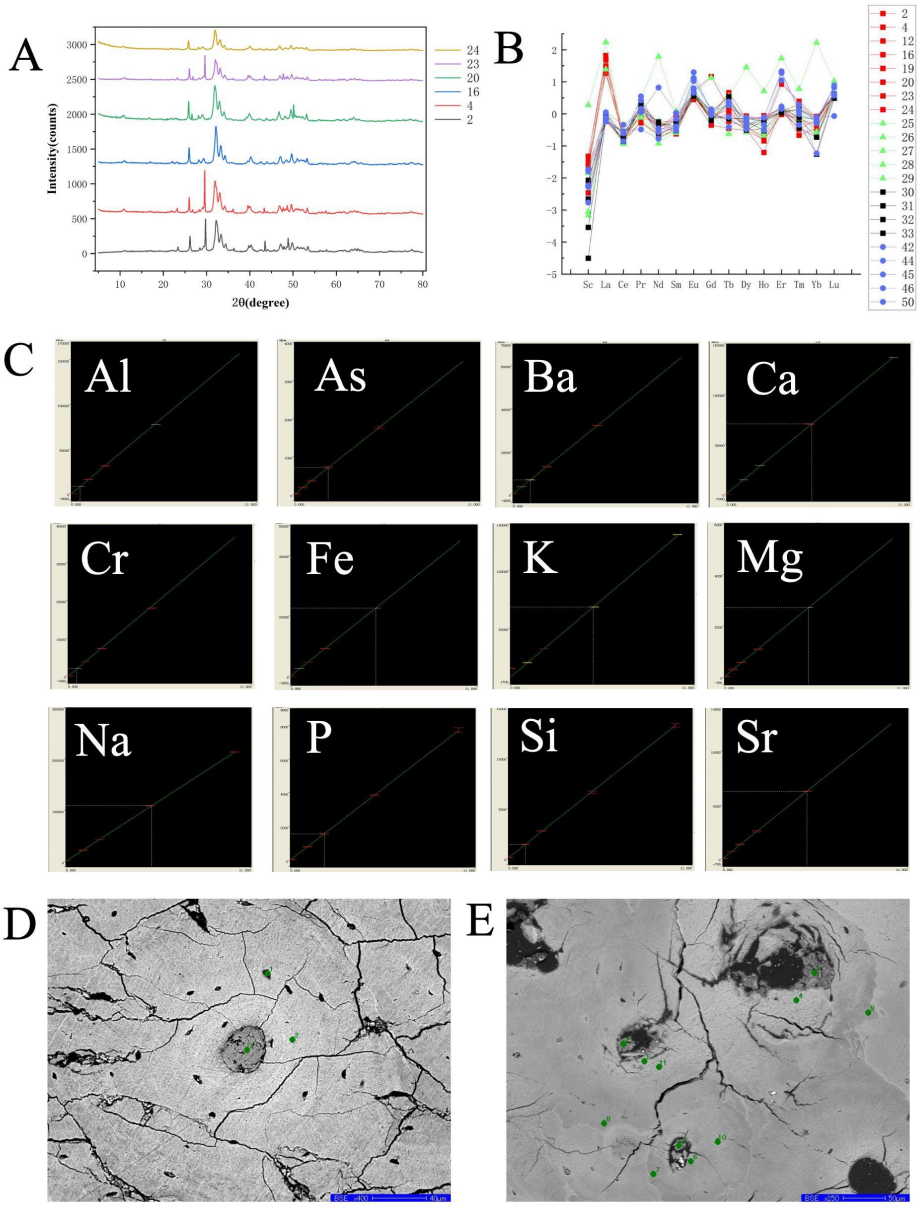

Figure 4 Characteristics of authentic *Os Draconis*. (A) XRD of 2, 4, 16, 20, 23, 24 authentic *Os Draconis*. These 6 samples were collected between 2022–2023 and were authenticated by ^{14}C; (B) spider plot of element; (C) Elemental standard curve; (D) Backscattered electron image of sample #4 (scale bar = 40 μm); (E) Backscattered electron image of sample #12 (scale bar = 50 μm). XRD, X-ray diffraction.

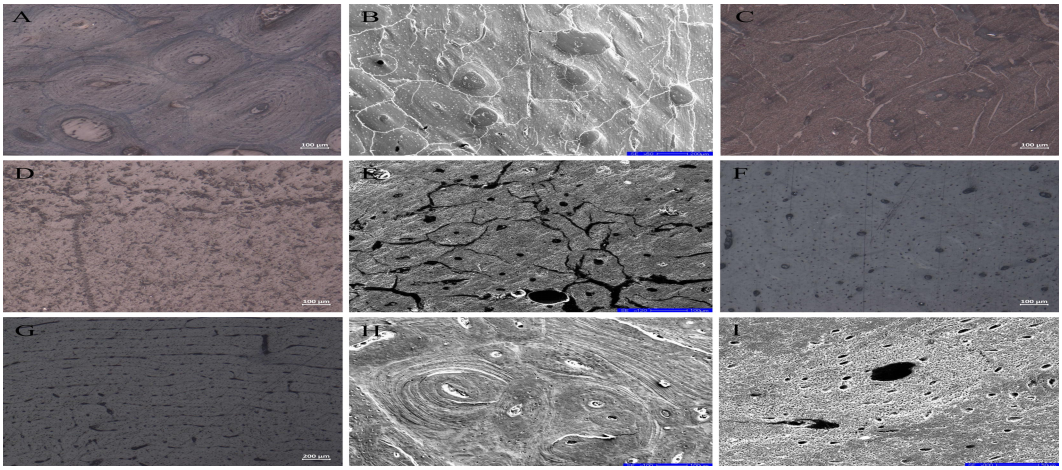

Figure 5 Characteristics of fossilized, counterfeit *Os Draconis* and lab-prepared *Os Draconis*. (A) polarized light microscopy image of fossilized *Os Draconis*; (B) Secondary electron image of fossilized *Os Draconis*; (C) polarized light microscopy image of counterfeit *Os Draconis*; (D) non-bone structure of polarized light microscopy image of counterfeit *Os Draconis*; (E) Secondary electron image of *Os Draconis* counterfeit *Os Draconis*; (F, G) polarized light microscopy image of lab-prepared samples; (H, I) Secondary electron image of lab-prepared samples.(scale bar: A, 100 μm; B, 200 μm; C–F, 100 μm; G, 200 μm; H, 100 μm; I, 50 μm).

In polarized microscopy, dense bone units of lab-prepared samples are round and tightly arranged; Haversian canals are mostly centered in the bone units, with distinct cement lines (Figure 5F). Some bone units exhibit unique arrangements, with multiple Haversian canals aligned in rows (Figure 5G). Secondary electron images show that, in samples of animal bone processed by boiling and low-temperature drying, dense bone units are round to elliptical and closely arranged, with Haversian canals centered and forming round or oval cavities. Bone lacunae are densely distributed around Haversian canals, with numerous lamellar layers in concentric rings. Bone units are intact, without fractures (Figure 5H). For calcined animal bone samples, bone units are blurred, and cement lines are no longer clear; due to high-temperature treatment, blood vessels and nerves in Haversian canals and bone lacunae have disappeared, forming voids; organic components like collagen fiber bundles in the Haversian lamellae have degraded, eliminating layered structures, while inorganic bone material has expanded, rendering the ultrastructure flat in electron probe images (Figure 5I).

XRD of fossilized, counterfeit *Os Draconis* and lab-prepared samples. The composition of fossilized *Os Draconis* is similar to *Os Draconis*, primarily containing hydroxyapatite and calcium carbonate. This result is consistent with electron probe analysis, with no quartz detected. Counterfeit samples only contain hydroxyapatite as a single phase. Lab-prepared samples of animal bone are also similar in phase composition to counterfeit samples, showing hydroxyapatite as the phase (Supplementary Table S3, Figure 6A–6C).

Ca/P ratio analysis. The elemental concentrations of Calcium (Ca) and Phosphorus (P) in fossilized *Os Draconis* (n = 5), counterfeit samples (n = 5), and lab-prepared animal bone samples (n = 6), as determined by ICP-MS, are detailed in Supplementary Table S4–S12, respectively. These data, along with those from authentic *Os Draconis* (n = 8) (Supplementary Table S7), were used to calculate the Ca/P molar ratio for each sample. The mean ± standard deviation (SD) Ca/P molar ratios for the groups were as follows: lab-prepared animal bone (1.34 ± 0.17), counterfeit samples (1.90 ± 0.06), authentic *Os Draconis* (2.23 ± 0.10), and fossilized *Os Draconis* (2.55 ± 0.36).

To determine if statistically significant differences existed in the observed mean Ca/P molar ratios among the different sample groups, a ANOVA was performed (total sample size N = 24; ANOVA degrees of freedom F (3, 20). To further identify which specific groups differed significantly from each other, Tukey's HSD post-hoc multiple comparisons test was conducted. The specific pairwise comparison results from Tukey's HSD test revealed that: the Ca/P ratio of lab-prepared animal bone was significantly lower than that of counterfeit samples ($P = 0.0006$), authentic *Os Draconis* ($P < 0.0001$), and fossilized *Os Draconis* ($P < 0.0001$). The Ca/P ratio of counterfeit samples was significantly lower than that of authentic *Os Draconis* ($P = 0.0350$) and fossilized *Os Draconis* ($P = 0.0002$). The Ca/P ratio of authentic *Os Draconis* was significantly lower than that of fossilized *Os Draconis* ($P = 0.0368$).

These statistically significant differences in Ca/P ratios highlight its importance as a distinguishing feature for samples from different origins. The Ca/P ratio of lab-prepared animal bone was significantly lower than that of all other three groups, aligning more closely with the theoretical values of biological apatite in fresh bone. The Ca/P ratio of counterfeit samples was significantly higher than that of lab-prepared bone but significantly lower than that of authentic and fossilized *Os Draconis*. The Ca/P ratio of authentic *Os Draconis* was, in turn, significantly lower than that of fossilized *Os Draconis*. The highest Ca/P ratio observed in fossilized *Os Draconis* may reflect diagenetic alterations that occurred during long-term burial, such as the relative loss of phosphate ions or the secondary enrichment of calcium-containing minerals (e.g., calcite). These results indicate that the Ca/P molar ratio, combined with statistical analysis, can be effectively used to aid in differentiating authentic *Os Draconis*, fossilized *Os Draconis*, counterfeit samples, and modern bones.

Elemental content distribution. From the 63 analyzed elements in all samples, authentic *Os Draconis* and fossilized *Os Draconis* have significantly lower Na, Mg, Si, K, Se, and Sn content compared to counterfeit and lab-prepared samples, while most other elements are generally higher. Mn content is notably higher in the former two than in the latter two. Specifically, Ca, P, Na, Mg, S, Sr, K, Ba, Al, Si, Fe, and Zn are relatively high, with Ca and P being the most prominent, with results shown in Supplementary Table S4–S6.

Rare earth elements refer to the group of rare earth elements from the lanthanide series, comprising 17 elements. The minerals from which these elements are extracted are relatively scarce, and their oxides are difficult to melt, poorly soluble in water, and hard to separate, earning them the nickname "industrial gold". This experiment analyzed 15 of these elements (Scandium (Sc), Lanthanum (La), Cerium (Ce), Praseodymium (Pr), Neodymium (Nd), Samarium (Sm), Europium (Eu), Gadolinium (Gd), Terbium (Tb), Dysprosium (Dy), Holmium (Ho), Erbium (Er), Thulium (Tm), Ytterbium (Yb), and Lutetium (Lu), and found a possible enrichment of La in authentic and fossilized *Os Draconis*. Sample 28#, collected in Qinghai Province, showed high levels of La, Nd, Sc, Gd, Dy, Er, and Yb in fossilized *Os Draconis*, whereas sample 27#, also from Qinghai, did not show this pattern, suggesting that further precise tracing of the origin may clarify regional effects on element distribution. However, it is important to acknowledge that with the current sample size, particularly when subdivided by geographical origin, definitive statistical conclusions about regional variations in specific elements

like Lanthanum (La) are limited by statistical power. While intriguing, these observations of potential regional differences in REE profiles, such as those noted between samples from Qinghai, should be considered preliminary and would require a larger, more geographically representative dataset for robust statistical validation. Future studies with expanded sampling across diverse geological provenances would be beneficial to rigorously assess the influence of origin on the elemental composition of *Os Draconis*.

In China, traditional Chinese medicine has a long history of using mineral drugs containing heavy metals for disease prevention and treatment, with efficacy and toxicity as its contradictory aspects. Currently, there are no specific regulations in China for heavy metal limits or quality control of mineral drugs. The existing standards such as *Chinese Pharmacopoeia* primarily address plant-based drugs. For example, the 2020 edition of the *Chinese Pharmacopoeia* sets limits for heavy metals and harmful elements, primarily covering lead (Pb), mercury (Hg), cadmium (Cd), copper (Cu), silver (Ag), bismuth (Bi), antimony (Sb), tin (Sn), and arsenic (As). For decoction pieces with established limits, lead should not exceed 5 mg/kg; cadmium, 1 mg/kg; arsenic, 2 mg/kg; mercury, 0.2 mg/kg; and copper, 20 mg/kg.

According to these standards, Cd and Cu in the four sample types meet the requirements, but all samples exceed the Hg limit. Pb and As in authentic and fossilized *Os Draconis* also exceed the limits. However, as mineral drugs, these limits do not apply to *Os Draconis*, indicating an urgent need for dedicated testing and verification to establish corresponding quality control standards. For the four sample types, Bi and Sb concentrations were around 0.3 mg/kg. Ag levels were higher in authentic and fossilized *Os Draconis* than in counterfeits and modern animal bones, while Sn levels were lower than in these two latter types.

EPMA analysis of different *Os Draconis*. It is known that the normal calcium-to-phosphorus (Ca/P) ratio in modern biological bones is approximately 2:1. This experiment analyzed 510 points, selecting 427 points with hydroxyapatite as the mineral phase for Ca/P ratio calculation. Among these, 24 batches of *Os Draconis* had 208 points, 5 batches of fossilized *Os Draconis* had 49 points, 12 batches of counterfeit bones had 89 points, and 9 batches of modern animal bone samples had 81 points. EPMA determined the Ca/P ratios of fossilized *Os Draconis*, counterfeit samples, and animal bones to be 3.32, 2.77, and 2.65, respectively, with all ratios exceeding 2 (Supplementary Table S7). Fossilized *Os Draconis* had the highest ratio, followed by authentic *Os Draconis*, and finally counterfeit and modern animal bones in descending order, aligning with the trends observed in ICP-MS elemental analysis results (Supplementary Table S8).

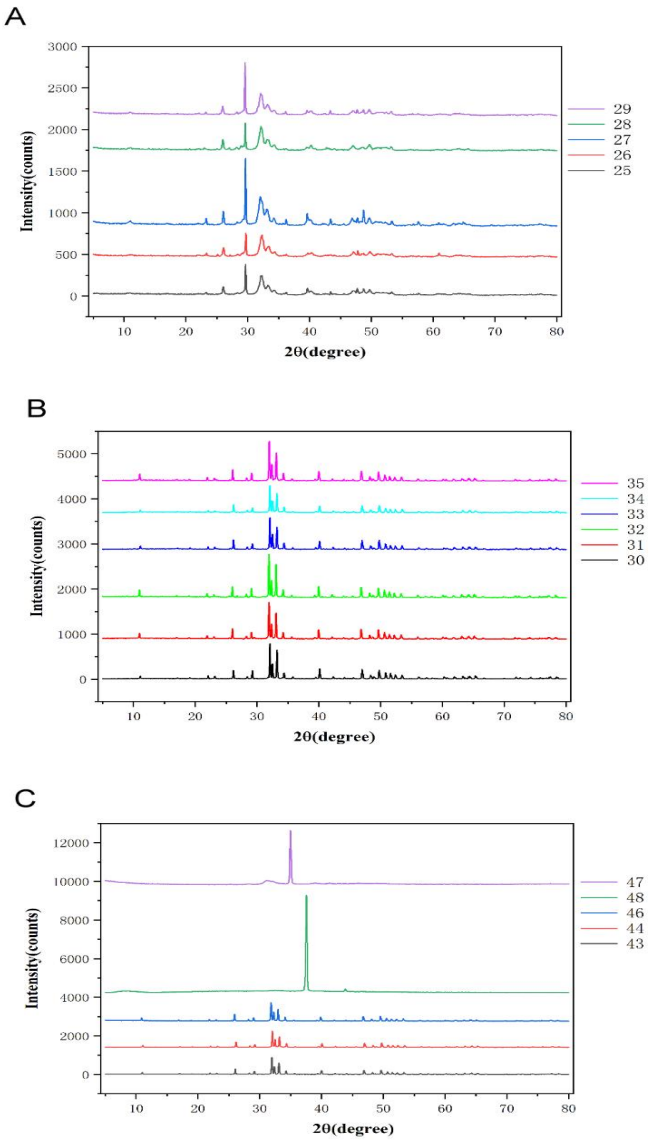

Figure 6 XRD result. The result of fossilized (A), counterfeit Os Draconis (B) and lab-prepared samples (C). XRD, X-ray diffraction.

Fossilized *Os Draconis* were analyzed at 63 points within the compact bone region, showing five mineral phases. Among these, 52 points had hydroxyapatite as the mineral phase, 7 points had calcite as a secondary calcium carbonate mineral, and 2 points contained Fe and Ba, with 1 point containing Cr and another representing a cavity (Supplementary Table S9). Hydroxyapatite accounted for 82.54% of the fossilized *Os Draconis*'s mineral phase and was primarily located within the lamellar bone. Calcite, the main secondary filling mineral, was found in six points within the Haversian canal and one point within a fissure. The points containing Fe and Ba were located within bone lacunae, showing brightness, while the Cr point was bright within the Haversian canal. No quartz filling was detected in fossilized *Os Draconis*. As shown in Figure 7A and Supplementary Table S10, point 1, located within the Haversian canal, was identified as calcite, while points 2–5 within the lamellar bone were all hydroxyapatite.

The counterfeit samples include 101 sites and six mineral phases; 90 sites contain hydroxyapatite, representing 89.1%, all located in bone lamellae. Five sites show quartz phases, with one site in a fracture, another in the Haversian canal of dense bone, and one in a pore in cancellous bone. Other sites include two voids, one wollastonite, two sites containing Fe, and one site containing Ba. No calcite phase of calcium carbonate was found (Supplementary Table S11). As shown in Figure 7B and Supplementary Table S12, Site 1 is located in the Haversian canal, with the mineral phase being calcite in the form of calcium carbonate. Sites 2–5 are located in the lamellar bone, and all have hydroxyapatite as the mineral phase.

For lab-prepared modern animal bone samples, there are 9 batches, with a total of 84 sites and two types of mineral phases, all located in the compact bone area. Among these, 81 sites are hydroxyapatite, accounting for 96.43% of the total. The remaining 3 sites are quartz, all found in the Haversian canal, and no calcite mineral phase of calcium carbonate was observed (Supplementary Table S13). As shown in Figure 7C and Supplementary Table S14, the 9 sites are all located in the lamellar bone with hydroxyapatite as the mineral phase. Site 2 contains sodium (Na) elements, and Sites 4 and 5 contain magnesium (Mg) elements.

Os Draconis analyzed by mercury intrusion porosimetry

Porosity refers to the ratio of the total pore volume to the apparent volume of a particle or powder [23]. It is a key parameter affecting fluid transport properties in porous media and is related to the shape, structure, and arrangement of solid particles in the medium. Total porosity is defined as the ratio of the pore volume (including both open and closed pores) to the total volume occupied by the solid. Pore structure is closely linked to the material's physical and chemical properties, making porosity an essential attribute for assessing the quality of pharmaceutical tablets. It directly impacts the mechanical properties, mass transfer, disintegration, dissolution, and bioavailability of tablets [24]. The mercury intrusion porosimetry method is widely applicable, covering pore diameters from 0.003 μm to 400 μm [25]. Since 1956, this technique has been extensively used in fields such as metallurgy and catalysis, and has also been applied to the pharmaceutical field abroad [26]. This experiment aims to study the basic physical characteristics of *Os Draconis* after geological processes by measuring physical parameters such as porosity, to investigate whether changes in pore size could influence the adsorption and release of other drugs.

In terms of porosity, authentic *Os Draconis* has a range between 30% and 47%, while fossilized *Os Draconis* ranges from 4% to 8%, with two samples (No. 25 and No. 26) around 25% and 30%, possibly due to incomplete filling in unique geological environments. Counterfeit samples range between 21% and 40%. Lab-prepared samples show two conditions: calcined samples exhibit significantly higher porosity than boiled or low-temperature dried samples. For example, the porosity of low-temperature dried bovine bone is 4.5847%, boiled bovine bone is 5.8721%, while calcined bovine bone rises to 17.4228%, and calcined goat bone reaches 40.4472%.

In terms of total pore area, authentic *Os Draconis* is between 25 and 70 m^2/g; fossilized *Os Draconis* is below 2 m^2/g, with two samples (No. 25–54.637 m^2/g and No. 26–39.783 m^2/g) exceptionally high. Counterfeit samples are also below 2 m^2/g, except for sample No. 30, which is unusually high at 31.405 m^2/g. Lab-prepared samples also show two categories, with calcined samples between 2 and 3 m^2/g, while boiled and low-temperature dried samples are both less than 1 m^2/g. The general trend shows that boiled and low-temperature dried bones of extant animals have the lowest pore area, which increases upon calcination. Counterfeits generally match the total pore area of calcined samples, while *Os Draconis* shows a significantly larger total pore area. Fossilized *Os Draconis* partially falls within the range of *Os Draconis* and partially matches that of counterfeit samples.

For median pore diameter, authentic *Os Draconis* ranges from 8 to 15 nm; fossilized *Os Draconis* is between 6 and 15 nm, with sample No. 29 exceptionally high at 230.54 nm. Counterfeit samples range from 150 to 280 nm, with sample No. 30 unusually low at 9.20 nm. Lab-prepared samples also show two conditions: calcined samples are around 220 nm, while boiled and low-temperature dried samples have median pore diameters of 7–8 nm. The trend is that boiled and low-temperature dried samples of extant animal bones have the smallest median pore diameter, which increases significantly after calcination. Counterfeits' median pore diameter is comparable to that of calcined samples, while *Os Draconis* has a median pore diameter slightly larger than boiled and low-temperature dried samples. Fossilized *Os Draconis*'s median pore diameter falls between that of *Os Draconis* and boiled or low-temperature dried samples of extant animal bones. According to IUPAC, pore diameters are classified as micropores (< 2 nm), mesopores (2–50 nm), and macropores (> 50 nm). Therefore, *Os Draconis* and fossilized *Os Draconis* belong to the mesopore range, while counterfeits and calcined samples of animal bones fall into the macropore range, and boiled and low-temperature dried samples also fall within the mesopore range.

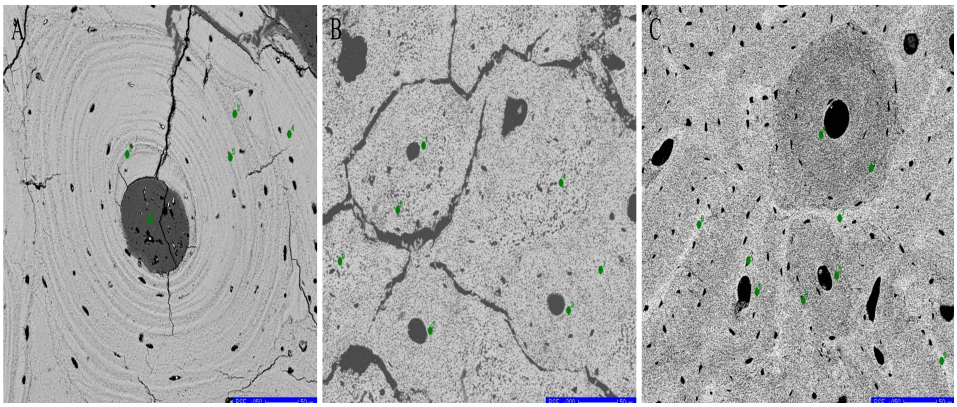

Figure 7 Backscattered electron image. (A) Backscattered electron image of sample #27 (Fossilized *Os Draconis*); (B) Backscattered electron image of sample #31 (counterfeit); (C) Backscattered electron image of sample #43 (lab-prepared sample) (scale bar = 50 μm).

The bulk density and apparent density of each sample type show a similar trend with minimal internal variation. The bulk density of authentic *Os Draconis* ranges from 1.3 to 1.8 g/mL, with an apparent density between 2.4 and 2.7 g/mL. Fossilized *Os Draconis* has a bulk density range of 1.7 to 2.7 g/mL, with an apparent density of 2.6 to 2.9 g/mL. Counterfeit samples have a bulk density between 1.4 and 2.2 g/mL, and an apparent density of 2.3 to 2.9 g/mL. Lab-prepared samples of boiled and low-temperature dried animal bones have a bulk density of approximately 1.6 to 2.4 g/mL, with an apparent density between 1.8 and 3.0 g/mL (Supplementary Table S15, Figure 8).

FTIR

The infrared spectra of *Os Draconis* primarily display characteristic absorptions of PO_4^{3-} and CO_3^{2-}, with fewer OH^- vibration bands (Figure 9, Supplementary Table S16).

For PO_4^{3-}: (1) Asymmetric stretching vibration (ν^{as}): This is the strongest absorption peak, ranging between 1,019–1,025 cm^{-1}. (2) Symmetric stretching vibration (ν^{s}): There is a distinct shoulder peak between 961–964 cm^{-1}. Counterfeit samples and lab-prepared samples also show a shoulder peak between 1,085–1,088 cm^{-1}. (3) Asymmetric bending vibration (δ^{as}): Two strong absorption bands appear at 599–601 cm^{-1} and 559–565 cm^{-1}. Counterfeit samples and lab-prepared samples additionally exhibit a shoulder peak around 630–632 cm^{-1}. (4) Symmetric bending vibration (δ^{s}): A weak absorption peak is present between 468–475 cm^{-1}.

CO_3^{2-}: Asymmetric stretching vibration (ν^{as}): Authentic *Os Draconis* and fossilized *Os Draconis* show two moderately strong absorption peaks (1,452–1,458 cm^{-1} and 1,412–1,425 cm^{-1}, with the 1,412–1,425 cm^{-1} peak slightly stronger). Pure reagent HAP exhibits two weak absorption bands of similar intensity in this range (Supplementary Table S17). Counterfeit samples and lab-prepared samples show a broad peak in this range (1,456–1,458 cm^{-1}), or the 1,452–1,458 cm^{-1} peak is slightly stronger than the 1,412–1,425 cm^{-1} peak. Some also show a third very weak absorption peak between 1,499–1,548 cm^{-1}. Out-of-plane bending vibration (γ): Authentic *Os Draconis* and fossilized *Os Draconis* exhibit a medium-strength absorption peak between 865–872 cm^{-1}. Pure reagent HAP has a weak absorption peak at 873 cm^{-1}. In counterfeit samples and lab-prepared samples, this weak absorption peak shifts toward lower frequencies (873–880 cm^{-1}). In-plane bending vibration (β): Authentic *Os Draconis* and fossilized *Os Draconis* show a distinct weak absorption peak between 712–714 cm^{-1}. In counterfeit samples and lab-prepared samples, this peak shifts to lower frequencies, appearing between 698–700 cm^{-1}, with reduced absorption intensity or sometimes undetectable.

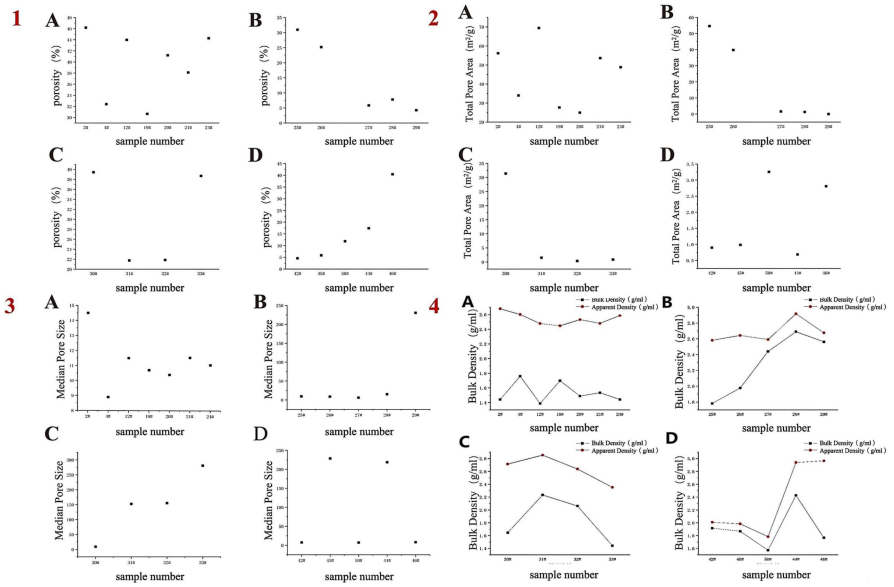

Figure 8 Differentiation of authentic and counterfeit *Os Draconis* based on physical property analysis. 1. Authentic *Os Draconis*; 2. fossilized *Os Draconis*; 3. Counterfeit; 4. Lab-prepared samples, (A) porosity (%), (B) surface area (m^2/g); (C) median pore size (nm); D. density.

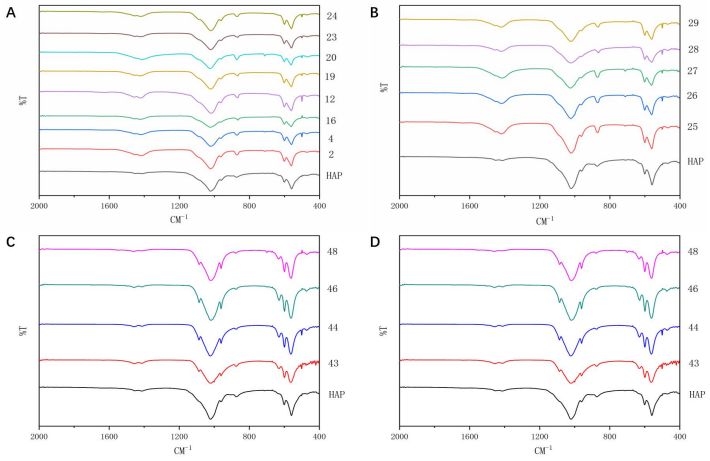

Figure 9 Fourier-transform infrared spectroscopy of *Os Draconis*. (A) Authentic *Os Draconis*; (B) fossilized *Os Draconis*; (C) Counterfeit; (D) Lab-prepared samples.

Discussion

Os Draconis, a type of fossil, has been used in traditional Chinese medicine since ancient times. In this study, multiple methods were applied to investigate the difference among authentic *Os Draconis*, fossilized *Os Draconis*, counterfeit and lab-prepared samples.

In paleontology, a fossil refers to the remains, traces, or organic residues (such as biomarkers and ancient DNA fragments) of organisms from geological history preserved in sediment due to natural processes. Fossils must exhibit certain biological characteristics, like shape, size, structure, and texture. Authentic *Os Draconis* primarily originates from Pliocene and Pleistocene mammalian fossils, approximately 12 million to 10,000 years ago. Based on literature review, this study defines fossilized vertebrate bone samples formed over 10,000 years ago as authentic *Os Draconis*. Animal bone samples formed within the past 10,000 years are considered counterfeit, while heavily mineralized samples unsuitable for medicinal use are classified as fossilized *Os Draconis*. Using ^{14}C dating, all samples in this experiment were analyzed to determine if they met fossil criteria, thereby confirming authenticity. Considering the low collagen content in *Os Draconis* due to complex geological processes, this study employed carbonate extraction dating. Results showed that authentic *Os Draconis* appears as intact bones or irregular fragments, sometimes with visible *Os Draconis* spots, though their absence does not necessarily indicate counterfeit. Fossilized *Os Draconis* is typically larger, heavily mineralized, dense, and hard to break, making it distinguishable from authentic samples. However, distinguishing small broken samples can be challenging. Counterfeits lack *Os Draconis* spots, exhibit complex shapes, and are often hygroscopic, making them sticky to the tongue, which can make verification challenging without sufficient experience. Lab-prepared samples of animal bones were created to simulate possible counterfeit steps using common mammalian bones (tibia from cow, goat, and pigs). Low-temperature dried and boiled samples exhibit an oily sheen and smell, while high-temperature calcined samples are brittle and light, making them easily distinguishable from authentic *Os Draconis*.

Authentic *Os Draconis* retains the macroscopic appearance of the original animal bone, but its internal microstructure has changed due to prolonged geological pressure and mineralization. In cross-sections of compact bone, many osteon structures appear round or irregular, with some forming irregular fissures that penetrate or traverse the osteon (a characteristic feature of authentic *Os Draconis*). These structural changes lead to cracking, deformation, displacement, and fusion of bone units. Osteons without fissures tend to remain circular, though varied in size, with occasional irregular deformations. Additionally, Haversian canals, which should be central to osteons, are often off-center or may appear as empty spaces. The lacunae in the bone matrix can either tightly encircle the Haversian canals or merge loosely with matrix pores, making osteon boundaries unclear. Secondary mineral deposits may appear in Haversian canals, lacunae, and gaps. Some counterfeits appear authentic in appearance but exhibit differences in microstructure. For instance, counterfeits created by calcination display fissures from thermal expansion along osteon cement lines, distinct from the fissures caused by geological compression. Lab-prepared samples lack clear cement lines and fissures, while fossilized *Os Draconis* shows expanded Haversian canals and prevalent fissures that penetrate osteons. In summary, examining the microstructural features of fissures within bone units can help distinguish authentic *Os Draconis* from other samples. Under polarized microscopy, it was observed that the diameters of bone units in *Os Draconis* vary significantly, ranging from 200 to 500 μm, while the diameters of Haversian canals range from 10 to 100 μm. Considering the limitations of the samples observed and the complexity of the original animals from which *Os Draconis* derives, future experiments are expected to use a larger sample size to obtain more reliable data, enabling a more accurate identification and pattern recognition within this data.

The primary mineral phase in authentic *Os Draconis* is hydroxyapatite, which is a key component of animal bone matrix. Based on XRD analysis, most of the detected calcium hydroxyapatite appears to be part of the original animal bone structure, classified as biogenic apatite. In contrast, samples with synthetic hydroxyapatite likely represent mineral substitution due to burial conditions. Among the 29 tested samples, only one-third showed a calcite mineral phase with calcium carbonate, indicating that not all samples contain calcium carbonate; this calcite likely also resulted from mineral replacement in the burial environment. However, there is currently no evidence that this serves as the pharmacologically active substance in *Os Draconis*. Quartz, one of the most common minerals on the Earth's surface, composed of silicon dioxide, is also likely to enter *Os Draconis* via geological replacement. Traditional wisdom holds that *Os Draconis* containing "dragon spots", referred as spot in this study, is considered high-quality; however, searches using "dragon spots" as a keyword or subject term yielded no relevant studies in current databases. These spots – ranging in size and varying in color from dark brown to black – appear as dotted, star-like, or branched patterns, sometimes on the *Os Draconis* surface and sometimes infiltrating internally. Based on morphology, these spots are likely calcite or quartz intrusions or replacements from the geological burial environment. Calcite crystal formation is influenced by supersaturation conditions during growth [27]. The morphology of magnesian calcite crystals depends on magnesium content and the degree of supersaturation at crystallization points [28]. Under high supersaturation, up to 15% $MgCO_3$ can be incorporated into calcite, forming spherical crystals. At lower supersaturation levels, the morphology transitions sequentially from spheres to dumbbells, to sheaf-like bundles, and finally to single crystals with steep rhombohedral faces. The historical emphasis on *Os Draconis* with "dragon spots" reflects the significance of geological timeframes in its formation.

Both genuine and substitute *Os Draconis* often exhibit soil-like impurities attached to the surface or within the trabecular spaces. These impurities primarily consist of magnesium calcite, muscovite, chabazite, dolomite, and montmorillonite. Radiocarbon dating of the impurities in one sample resulted in an age of 3,620 ± 30 BP, indicating an age of less than 10,000 years, which contrasts with the over 35,000-year age (35,980 ± 330 BP) of ancient *Os Draconis*, suggesting a later adherence or occupation. Though one sample may not be representative, further studies are required. The distribution of mineral phases in *Os Draconis* does not exhibit a clear pattern based on geographic origin. The formation and distribution of mineral phases are influenced by various factors, including but not limited to geographical location, geological structure, climate, hydrological conditions, and soil type. While geography may not show a straightforward influence on mineral phases, further exploration may reveal associations.

Current research on the chemical composition of *Os Draconis* primarily focuses on quantitative analysis of calcium (Ca), identifying hydroxyapatite and calcium carbonate ($CaCO_3$) as its main components, along with some undefined impurities. Additionally, quantitative analysis of heavy metals (e.g., Pb, Cr, Cd, As, Hg, Cu), radioactive elements (U, Th), and other trace elements lacks a consistent summary due to uncertain sample dating. XRD results in this study show that authentic *Os Draconis* consists predominantly of hydroxyapatite, with some samples containing calcium carbonate and quartz. Geographic origin does not appear to significantly influence mineral phases. Samples containing "dragon spots" feature quartz and magnesian calcite in addition to hydroxyapatite, while no calcium carbonate was detected in imitation or lab-prepared animal bone samples, which consist mainly of hydroxyapatite. ICP-MS analysis reveals that authentic *Os Draconis* is relatively enriched in lanthanum (La), europium (Eu), erbium (Er), and lutetium (Lu) compared to the mantle, with a significant depletion in scandium (Sc), while other elements show slight depletion, likely due to burial and fossilization processes. Analysis indicates a Ca/P ratio of 2.23, higher than the standard hydroxyapatite value of 1.67. Due to differences in radius and bond valency, Ca^{2+} ions in hydroxyapatite can be replaced by various metal ions, giving it strong ion exchange capability. The Ca/P

molar ratio can be adjusted through acidic or basic active sites, with values below or above 1.67 favoring acidic or basic catalysis, respectively, suggesting its potential application in catalysis [29]. Thus, *Os Draconis* could be viewed as a natural basic catalytic material. Although trace elements exist in low quantities, they play crucial roles in cell metabolism, enzyme activity regulation, immune function, neural transmission, and bone health. However, further investigation is needed to determine if *Os Draconis*'s medicinal properties arise from the combined effects of its trace elements, which minerals are pharmacologically active, and the mechanisms behind its efficacy. Harmful elements were also detected in *Os Draconis*. Its main component, hydroxyapatite, belongs to the hexagonal crystal system, allowing various ions to substitute within its crystal lattice [30]. Therefore, it's inferred that *Os Draconis* can adsorb and concentrate surrounding crustal elements during formation, an important consideration for future quality standards and medicinal use.

EPMA phase analysis shows that the microcomposition of authentic *Os Draconis* aligns with XRD results, consisting primarily of hydroxyapatite, with secondary minerals like calcite and quartz occasionally filling haversian canals, lacunae, and cracks. The average Ca/P ratio calculated from EPMA results is 2.92, suggesting that hydroxyapatite forms the main substance of *Os Draconis*, with mineral filling and replacement initially occurring in pores and fractures and then gradually permeating the bone substance. Some counterfeit samples closely resemble authentic *Os Draconis* in appearance, but differences emerge at the ultrastructural level. Certain imitations show fractures due to calcination; however, these fractures, caused by thermal expansion, split along bone unit adhesion lines, differing from the geologically induced fractures that penetrate bone units. Lab-prepared animal bone samples display unclear adhesion lines and no fractures. In fossilized *Os Draconis*, haversian canals are sometimes filled and expanded or compressed into points, with fractures often extending into or through bone units. Thus, ultrastructural observation of bone unit fractures can distinguish authentic *Os Draconis* from other samples.

The phase results from XRD and EPMA show that counterfeit and laboratory-prepared modern animal bones consist mainly of hydroxyapatite. EPMA findings indicate that secondary filling minerals are often located in pores such as haversian canals and lacunae, with authentic *Os Draconis* having the most diverse types of secondary fillers, primarily calcium carbonate and quartz. Fossilized *Os Draconis* contains fewer types of secondary fillers than authentic *Os Draconis*, with no quartz detected thus far. Counterfeit and modern animal bone samples show minimal filling. These results suggest that hydroxyapatite is the primary substance in animal bones, while the presence of calcium carbonate calcite in *Os Draconis* and fossilized *Os Draconis* results from the gradual accumulation and replacement of crustal elements during fossilization.

ICP-MS analysis shows that the Ca/P ratios for fossilized *Os Draconis* (2.55), *Os Draconis* (2.23), counterfeit samples (1.90), and animal bone samples (1.97) are all greater than that of standard hydroxyapatite (1.67). EPMA results yield Ca/P ratios of 3.32, 2.92, 2.77, and 2.65, respectively. It's speculated that the substitution of calcium carbonate calcite during geological burial increased the calcium ratio. A larger sample size in future studies could allow for statistical range determination to help distinguish different types of samples. The results from both techniques show a similar trend, with the Ca/P ratio of authentic *Os Draconis* falling between that of fossilized *Os Draconis* and counterfeit samples, providing a potential compositional distinction.

The significant enrichment of certain rare earth elements (REEs), notably Lanthanum (La), alongside Europium (Eu), Erbium (Er), and Lutetium (Lu) in authentic *Os Draconis* (Figure 4B), as revealed by ICP-MS, invites discussion on their potential contribution to its traditional pharmacological effects, particularly its sedative and tranquilizing actions. Pharmacologically, La^{3+} is known to interact with Ca^{2+} channels due to ionic similarities [31]. Given Ca^{2+}'s role in neuronal excitability, it is hypothesized that enriched La in *Os Draconis* might modulate central nervous system activity, contributing to its calming effects. However, this link is currently speculative. The chemical form of these REEs, their leachability during traditional preparation, and subsequent bioavailability are critical unknowns. Future research should investigate these aspects and conduct targeted pharmacological studies to determine if REEs, at physiologically relevant concentrations, indeed mediate the neurological effects of *Os Draconis*. Elucidating this could deepen our understanding of the material basis for the efficacy of this mineral medicine.

The elevated levels of heavy metals such as Mercury (Hg), Lead (Pb), and Arsenic (As) detected in authentic and fossilized *Os Draconis* samples (Supplementary Table S4–S12) necessitate careful consideration of their potential toxicity and implications for clinical application. While these elements are known toxicants with established adverse effects on various organ systems, their presence in mineral medicines like *Os Draconis*, which has a long history of traditional use, presents a complex issue. The actual risk posed depends significantly on their chemical speciation (e.g., inorganic vs. organic forms, solubility), leachability during traditional preparation, and subsequent bioavailability in the human body – factors that are currently not well understood for *Os Draconis*.

Although current pharmacopoeia limits primarily target plant-based medicines and may not be directly applicable, the observed concentrations, particularly for Hg, Pb, and As exceeding these general thresholds, underscore the urgent need for dedicated safety assessments and specific quality control standards for mineral TCMs. Clinically, this implies a cautious approach, potentially involving batch-to-batch testing, adherence to recommended dosages and treatment durations, and further research to establish a clearer benefit-risk profile, especially for long-term or high-dose applications. Future studies should aim to quantify the bioaccessible fraction of these heavy metals from *Os Draconis* under conditions mimicking human digestion and explore processing methods that might mitigate potential risks.

The infrared spectroscopy results indicate clear differences in the apatite contained in *Os Draconis* compared to that in counterfeit samples, lab-prepared samples of modern animal bones, and pure HAP reagent. The infrared spectrum of *Os Draconis* primarily shows characteristic absorption of PO_4^{3-} and CO_3^{2-}, with fewer OH^- vibration bands. In contrast, counterfeit samples, laboratory-made products, and pure HAP also exhibit the PO_4^{3-} absorption, but with significantly weakened or even undetectable CO_3^{2-} absorption. This finding aligns with the XRD and EPMA composition analyses, suggesting that CO_3^{2-} can be used as a distinguishing point for identifying *Os Draconis* via infrared spectrum. However, it is crucial to acknowledge that CO_3^{2-} was not universally present in all samples identified as authentic *Os Draconis* (OA) in this study, with some OA samples exhibiting weak or absent CO_3^{2-} signals. The lack of a strong CO_3^{2-} signal in these authentic samples could be attributed to various factors, including variations in the original burial environment which influence carbonate substitution and preservation. This observation underscores that while CO_3^{2-} provides valuable information, relying solely on its presence for the authentication of *Os Draconis* may not be sufficiently robust. Therefore, in the future, multi-marker panels – for example, combining CO_3^{2-} detection with assessments of quartz presence and porosity/microstructural features – could better account for the inherent heterogeneity of *Os Draconis* and provide a stronger basis for distinguishing authentic samples from fossilized specimens not intended for medicinal use and various counterfeits.

Although processed calcium carbonate can have high bioavailability, there is no evidence that it constitutes the active medicinal component of *Os Draconis*. Furthermore, there is no definitive proof that CO_3^{2-} exists solely as $CaCO_3$ in *Os Draconis*. Currently, CO_3^{2-} in hydroxyapatite is thought to have two substitution types, A-type and B-type [32]. A-type CO_3^{2-} exhibits double peaks around 1,545 cm^{-1}, 1,450 cm^{-1}, and 880 cm^{-1}, while B-type occurs around 1,455 cm^{-1}, 1,410 cm^{-1}, and 875 cm^{-1}. This suggests that in *Os Draconis*, B-type CO_3^{2-} substitution replaces PO_4^{3-} tetrahedra. Rey et al. propose that in bone minerals, CO_3^{2-} substitutes OH^- in the apatite structure, resulting in little or no OH^- [33]. Kazuki Oguri et al. suggest that

during decoction, *Os Draconis* not only releases its components but also absorbs ingredients from other herbs [34, 35]. Given that HAP can adsorb various materials, it has been studied as a carrier in drug delivery systems. Based on the experimental results in this chapter, *Os Draconis* could be considered a natural drug carrier, due to two key factors: its appropriately sized pore diameters and surface area, which support the distribution of other medicinal components, and its crystal structure and binding sites, which favor the adsorption of charged ions.

Conclusion

In conclusion, this study successfully established a multi-analytical approach combining ^{14}C dating, microstructural analysis (PLM, EPMA-SEM), and compositional characterization (XRD, FTIR, ICP-MS, EPMA-WDS) to reliably differentiate authentic *Os Draconis* from its fossilized counterparts and counterfeits. Key discriminators include the presence of calcite and specific carbonate FTIR bands, distinct crack patterns penetrating osteons, higher Ca/P ratios, and unique rare earth element enrichment patterns (notably La) in authentic samples. Furthermore, the inherent porosity suggests potential as a natural drug carrier.

Moving forward, several avenues of research are crucial. First, elucidating the pharmacological mechanisms underlying the traditional efficacy of *Os Draconis*, particularly its sedative and tranquilizing effects, is paramount. This should involve investigating the potential contribution of enriched trace elements, especially rare earths like Lanthanum (La), by exploring their interactions with relevant neurological pathways and assessing their bioavailability from the *Os Draconis* matrix. Second, a thorough toxicity evaluation is urgently needed, focusing on the identified heavy metals (Hg, Pb, As). Research should determine their chemical speciation, bioaccessibility under physiological conditions and traditional preparation methods, and establish evidence-based safety limits specific to *Os Draconis* as a mineral medicine, moving beyond standards set for plant-based drugs. Finally, further investigation into its properties as a drug delivery vehicle, including loading capacity, release kinetics for various drug types, and in vivo biocompatibility, would be valuable for exploring novel applications.

References

1. Anthony EJ, Bolitho EM, Bridgewater HE, et al. Metallodrugs are unique: opportunities and challenges of discovery and development. *Chem Sci*. 2020;11(48):12888–12917. Available at: https://doi.org/10.1039/D0SC04082G
2. Chen Y, Xiong W, Zhang Y, et al. Carbon dots derived from os draconis and their anxiolytic effect. *Int J Nanomedicine*. 2022;17:4975–4988. Available at: https://doi.org/10.2147/IJN.S382112
3. Yang DD, Chen HB. Treatment of insomnia based on the midnight-noon ebb-flow. *J Tradit Chin Med*. 2010;30(3):228–231. Available at: https://doi.org/10.1016/S0254-6272(10)60046-5
4. Lee TMY, Guo L, Shi H, et al. Neural correlates of traditional Chinese medicine induced advantageous risk-taking decision making. *Brain Cogn*. 2009;71(3):354–361.Available at: https://doi.org/10.1016/j.bandc.2009.06.006
5. Jia XR, Chen J, Huang RO, et al. Effect-enhancing and toxicity-reducing effects of Chaihu Jia Longgu Muli decoction in the treatment of multimorbidity with depression: a systematic review and meta-analysis. *Pharm Biol*. 2023;61(1):1094–1106. Available at: https://doi.org/10.1080/13880209.2023.2228356
6. Wang BF, Teng Y, Li Y, et al. Evidence and characteristics of traditional Chinese medicine for coronary heart disease patients with anxiety or depression: a meta-analysis and systematic review. *Front Pharmacol*. 2022;13:854292. Available at: https://doi.org/10.3389/fphar.2022.854292
7. Dang C, Wang QX, Li Q, Xiong Y, Lu YH. Chinese herbal medicines for the treatment of depression: a systematic review and network meta-analysis. *Front Pharmacol*. 2024;15:1295564. Available at: https://doi.org/10.3389/fphar.2024.1295564
8. Li LF, Lu J, Li XM, et al. Antidepressant-like effects of the saponins extracted from Chaihu-jia-longgu-muli-tang in a rat unpredictable chronic mild stress model. *Fitoterapia*. 2012;83(1):93–103. Available at: https://doi.org/10.1016/j.fitote.2011.09.017
9. Li C, Li B, Liu H, Qu L, Wang H. Mechanism of Chaihu Longgu oyster adjusted decoction for the treatment of depression based on network pharmacology and molecular docking technology. *Ann Transl Med*. 2023;11(4):172. Available at: https://doi.org/10.21037/atm-23-236
10. Xia S, Yang P, Li F, et al. Chaihu-Longgu-Muli Decoction exerts an antiepileptic effect in rats by improving pyroptosis in hippocampal neurons. *J Ethnopharmacol*. 2021;270:113794. Available at: https://doi.org/10.1016/j.jep.2021.113794
11. Wang X, Ju J, Li J, Fan Y, Xu H. Chaihu Longgu Muli decoction, a Chinese herbal formula, for the treatment of insomnia. *Medicine (Baltimore)*. 2020;99(40):e22462. Available at: https://doi.org/10.1097/MD.0000000000022462
12. Yu M, Jia HM, Zhang T, et al. Gut Microbiota Is the Key to the Antidepressant Effect of Chaihu-Shu-Gan-San. *Metabolites*. 2020;10(2):63. Available at: https://doi.org/10.3390/metabo10020063
13. Oguri K, Ueda T, Takahashi K. Transition in Longgu Surface Associated with Decoction Process of Keishikaryukotsuboreito. *Chem Pharm Bull*. 2019;67(7):693–698. Available at: https://doi.org/10.1248/cpb.c18-00866
14. Guan HF, Xu Y, Ma CY, Zhao DX. Pharmacology, toxicology, and rational application of cinnabar, realgar, and their formulations. *Evid Based Complement Alternat Med*. 2022;2022(1):6369150. Available at: https://doi.org/10.1155/2022/6369150
15. Lao LX, Huang Y, Feng CG, Berman BM, Tan MT. Evaluating traditional Chinese medicine using modern clinical trial design and statistical methodology: application to a randomized controlled acupuncture trial. *Stat Med*. 2012;31(7):619–627. Available at: https://doi.org/10.1002/sim.4003
16. Tian YW, Shi Y, Zhu YJ, et al. The modern scientific mystery of traditional Chinese medicine processing – take some common traditional Chinese medicine as examples. *Heliyon*. 2024;10(2):e25091. Available at: https://doi.org/10.1016/j.heliyon.2024.e25091
17. Wu LY, Wu QF, Du XT, Ling ML, Tong HB. Revolutionizing pharmacological research of traditional Chinese medicine with single-cell omics technologies. *Fitoterapia*. 2025;186:106846. Available at: https://doi.org/10.1016/j.fitote.2025.106846
18. Chinese Materia Medica Commission. *Chinese Materia Medica*. Shanghai, China: Shanghai Science and Technology Press; 1999. Available at: ISBN: 9787506773379
19. Kang TG. *Chinese Medicine Identification*. Beijing, China: China Press of Traditional Chinese Medicine; 2016. Available at: ISBN: 9787513234122
20. Chui SH, Wong YH, Chio HI, et al. Study of heavy metal poisoning in frequent users of Chinese medicines in Hong Kong and Macau. *Phytother Res*. 2013;27(6):859–863. Available at: https://doi.org/10.1002/ptr.4816
21. von Wandruszka R, Warner MS. Recognizing and Analyzing Chinese Stone Drugs. *Hist Archaeol*. 2021;55(4):597–605. Available at: https://doi.org/10.1007/s41636-021-00306-3

22. Bai DH, Xing Z, Zhang ZH, et al. Ultrastructure and key identification points of fossilized *Os Draconis* in traditional Chinese medicine. *Tradit Med Res.* 2026;11(1):3. Available at: https://doi.org/10.53388/TMR20241113001
23. Qiu J, Khalloufi S, Martynenko A, Van Dalen G, Schutyser M, Almeida-Rivera C. Porosity, Bulk Density, and Volume Reduction During Drying: Review of Measurement Methods and Coefficient Determinations. *Dry Technol.* 2015;33(14): 1681–1699. Available at: https://doi.org/10.1080/07373937.2015.1036289
24. Teixeira MT, Sa-Barreto LL, Silva IC, et al. The influence of porosity on tablet subdivision. *Particuology.* 2020;53:192–196. Available at: https://doi.org/10.1016/j.partic.2020.06.001
25. y Leon CAL. New perspectives in mercury porosimetry. *Adv Colloid Interface Sci*. 1998;76–77:341–372. Available at: https://doi.org/10.1016/S0001-8686(98)00052-9
26. Kim JW, Cheon YH, Donchev D, et al. Investigation of entrapped pore in the pastilles by a mercury porosimetery technique. *Int J Pharm*. 2005;288(2):305–314. Available at: https://doi.org/10.1016/j.ijpharm.2004.10.018
27. Kile DE, Eberl DD, Hoch AR, et al. An assessment of calcite crystal growth mechanisms based on crystal size distributions. *Geochim Cosmochim Acta*. 2000;64(17):2937–2950. Available at: https://doi.org/10.1016/S0016-7037(00)00394-X
28. Fernandez-Diaz L, Putnis A, Prieto M, Putnis CV. The role of magnesium in the crystallization of calcite and aragonite in a porous medium. *J Sediment Res.* 1996;66(3):482–491. Available at: https://doi.org/10.1306/D4268388-2B26-11D7-8648000102C1865D
29. Mekmene O, Quillard S, Rouillon T, et al. Effects of pH and Ca/P molar ratio on the quantity and crystalline structure of calcium phosphates obtained from aqueous solutions. *Dairy Sci Technol*. 2009;89(3):301–316. Available at: https://doi.org/10.1051/dst/2009019
30. Ratnayake JTB, Mucalo M, Dias GJ. Substituted hydroxyapatites for bone regeneration: A review of current trends. *J Biomed Mater Res B Appl Biomater*. 2017;105(5):1285–1299. Available at: https://doi.org/10.1002/jbm.b.33651
31. Yang J, Elllnor PT, Sather WA, Zhang JF, Tsien RW. Molecular determinants of Ca^{2+} selectivity and ion permeation in L-type Ca^{2+} channels. *Nature.* 1993;366(6451):158–161. Available at: https://doi.org/10.1038/366158a0
32. Astala R, Stott MJ. First principles investigation of mineral component of bone: CO_3 substitutions in hydroxyapatite. *Chem Mater.* 2005;17(16):4125–4133. Available at: https://doi.org/10.1021/cm050523b
33. Rey C, Collins B, Goehl T, Dickson IR, Glimcher MJ. The carbonate environment in bone mineral: A resolution-enhanced fourier transform infrared spectroscopy study. *Calcif Tissue Int.* 1989;45(3):157–164. Available at: https://doi.org/10.1007/BF02556059
34. Oguri K, Kawase M, Harada K, Shimada-Takaura K, Takahashi T, Takahashi K. Longgu (Fossilia Ossis Mastodi) alters the profiles of organic and inorganic components in Keishikaryukotsuboreito. *J Nat Med.* 2016;70(3):483–491. Available at: https://doi.org/10.1007/s11418-015-0952-2
35. Bai D, Nowak M, Lu D, et al. The outcast of medicine: metals in medicine – from traditional mineral medicine to metallodrugs. *Front Pharmacol.* 2025;16:1542560. Available at: https://doi.org/10.3389/fphar.2025.1542560